Two cryptic anatectic events within a syn-collisional granitoid from the Araçuaí orogen (southeastern Brazil): Evidence from the polymetamorphic Carlos Chagas batholith

M.G. Melo [a,b,*], G. Stevens [b], C. Lana [a,1], A.C. Pedrosa-Soares [c,1], D. Frei [b], F.F. Alkmim [a,1], L.A. Alkmin [a]

[a] Applied Isotope Research Group, Departamento de Geologia, Escola de Minas, Universidade Federal de Ouro Preto, Campus Universitário Morro do Cruzeiro s/n, 35400-000 Ouro Preto, MG, Brazil
[b] Centre for Crustal Petrology, Department of Earth Sciences, Stellenbosch University, Private Bag X1, Matieland 7602, South Africa
[c] Universidade Federal de Minas Gerais, IGC–CPMTC, Campus Pampulha, 31270-901 Belo Horizonte, MG, Brazil

ARTICLE INFO

ABSTRACT

From the earliest (ca. 630 Ma) pre-collisional plutons to the latest (ca. 480 Ma) post-collisional intrusions, the Araçuaí orogen (SE Brazil) records an outstanding succession of granite production events in space and time. The Carlos Chagas batholith (CCB) is the largest (~14,000 km^2) granitic body ascribed to the collisional plutonism (G2 supersuite) in the back-arc region of the Araçuaí orogen, to the east of the Rio Doce magmatic arc. A wide range of monazite and zircon ages (>725 Ma to ca. 490 Ma) have been found in CCB granites, recording a rich history of crustal recycling and inheritance, magmatic crystallization and anatexis. The CCB includes a dominant granite richer in garnet than in biotite, in which three mineral assemblages can be identified: 1) Qz + Pl + Kfs + Bt + Grt + Ilm ± Rt; 2) Qz + Pl + Kfs + Bt + Grt + Ilm + Sil; and 3) Qz + Pl + Kfs + Bt + Grt + Ilm + Sil + Spl. Rocks which contain mineral assemblage 2 and 3 all contain two generations of garnet. Textural evidence for the presence of former melt, recognized in all studied CCB samples, includes: silicate melt inclusions in poikiloblastic garnet, pseudomorphed thin films of melt surrounding both generations of garnet, pseudomorphed melt pools adjacent to garnet and biotite, and plagioclase and quartz with cuspate-lobate shapes occurring among matrix grains. Both generations of garnet crystals (Grt$_1$ and Grt$_2$) are unzoned in terms of major element concentration, contain small rounded inclusions of Ti-rich biotite and, in addition, the Grt$_2$ crystals also contain inclusions of remnant sillimanite needles. Microstructural evidence, in combination with mineral chemistry, indicates that the garnet crystals grew during two distinct metamorphic-anatectic events, as the peritectic products of fluid-absent melting reactions which consumed biotite, quartz and plagioclase, in the case of Grt$_1$, and which consumed biotite, quartz, plagioclase and sillimanite in the case of Grt$_2$. P–T pseudosections calculated via Theriak-Domino, in combination with in situ U–Pb monazite and zircon dating, provide new constraints on the thermal evolution of the back-arc region of the Araçuaí orogen. Data from assemblage 1 suggests P–T conditions for the first granulite-facies metamorphic event (M1) at 790–820 °C and 9.5–10.5 kbar, while the assemblage 2 records P–T conditions for a second granulite-facies metamorphism (M2) of around 770 °C and 6.6 kbar. Monazite and zircon within garnets from the different assemblages give age peaks at 570–550 Ma (M1) and 535–515 Ma (M2), recording two anatectic events in the CCB during a single orogenic cycle. The PT conditions for these metamorphic events can be related to: i) M1, striking crustal thickening, probably involving thrusting of the magmatic arc onto the back-arc region; and ii) M2, decompression related to the gravitational collapse of the Araçuaí orogen.

© 2016 Elsevier B.V. All rights reserved.

1. Introduction

Crustal differentiation is an important process in the stabilization of the continental crust. There is widespread consensus that the rocks forming the lower continental crust record at least one cycle of partial melting (>800 °C; e.g. Brown, 1994, 2010). The resultant granitic magmas migrate upwards, enriching the upper crust in SiO$_2$, K$_2$O and Na$_2$O, and leaving the lower crust dehydrated, more refractory and enriched in Al$_2$O$_3$, FeO, MgO and CaO (Brown, 2013; Brown and Rushmer, 2006; Petford et al., 2000).

* Corresponding author at: Applied Isotope Research Group, Departamento de Geologia, Escola de Minas, Universidade Federal de Ouro Preto, Campus Universitário Morro do Cruzeiro s/n, 35400-000 Ouro Preto, MG, Brazil.
E-mail addresses: marilanegonzaga@hotmail.com (M.G. Melo), pedrosasoares@ufmg.br (A.C. Pedrosa-Soares).
[1] Fellow of the Brazilian Research Council (CNPq).

In long-lived orogenic systems some rocks may record more than one cycle of tectonic burial with partial melting at depth (Jeon et al., 2012; Richter et al., 2016). Likewise, early orogenic granites (sensu lato), emplaced into the upper crust, may be buried together with overlying sedimentary and volcanic sequences to lower crustal levels, and recycled in the lower crust as the orogeny evolves. This recurring process of partial melting may have contributed to the formation of vast amounts of S-type granite and has been documented in a number of orogenic systems, such as the Lachlan fold belt (Chappell and White, 1974), the Araçuaí Orogen (Pedrosa-Soares et al., 2001, 2011), and the Tasmanide orogenic system (Collins and Richards, 2008).

In the Ediacaran-Cambrian Araçuaí orogen, there is evidence of at least three regional anatectic events that formed the S-type granites included in the G2 (ca. 585–545 Ma), G3 (ca. 545–530 Ma) and G4 supersuites (ca. 530–500 Ma) (De Campos et al., 2004, 2016; Gradim et al., 2014; Pedrosa-Soares et al., 2001, 2011; Richter et al., 2016; Tedeschi et al., 2016). No previous studies have investigated the potential anatectic recycling of older granites through detailed study of their mineralogy, mineral textures, mineral chemistry and geochronology. This study investigates the petrogenesis of the Carlos Chagas batholith (CCB), a very large body (~14,000 km^2) composed of peraluminous, S-type granites that formed during the syn-collisional stage of the Araçuaí orogen, with a view to better understanding crustal recycling during a long-lived orogeny. We present new petrographic evidence, as well as major and trace element mineral chemistry which documents garnet growth during two separate partial melting episodes in the CCB. U–Pb in situ monazite and zircon dating allow the timing of the high-grade metamorphic events that produced the garnet crystals to be constrained. In addition, P–T–t paths for the two successive metamorphic events are quantified in order to explain how granitic bodies, possibly initially intruded into the upper crust, can experience more than one cycle of mid- to lower crustal tectonic recycling.

2. Geotectonic and regional setting

The Araçuaí orogen of southeastern Brazil together with its counterpart located in southwestern Africa, the West Congo belt (Fig. 1), form an orogenic system that developed during the Brasiliano–Pan-African orogeny between the São Francisco and Congo cratons (Alkmim et al., 2006; Pedrosa-Soares et al., 2001, 2008). Formed during the amalgamation of Western Gondwana in Ediacaran to Cambrian time, the Araçuaí-West Congo orogenic system was split into two distinct belts by the opening of the South Atlantic Ocean in the Cretaceous (Fig. 1). The West Congo belt inherited important rift to proximal passive margin sequences of the precursor basins, which show low grade metamorphism and no orogenic igneous rocks (Tack et al., 2001). On the other hand, the Araçuaí orogen inherited two thirds of the orogenic system, including rift-related to distal passive margin and oceanic sequences with ophiolitic bodies of the precursor basin system, and the Rio Doce magmatic arc, as well as the collisional and post-collisional igneous suites (Pedrosa-Soares et al., 2001, 2008, 2011). The huge quantity of orogenic granites in the Araçuaí orogen can be grouped into five regional supersuites based on field relationships, structural features and geochemical and geochronological data. These are: G1 (Rio Doce magmatic arc, ca. 630–585 Ma), G2 (ca. 585–545 Ma), G3 (ca. 545–530 Ma), G4 (ca. 530–500 Ma), and G5 (ca. 525–480 Ma) (see synthesis, and updated geochemical and geochronological data in Belém, 2014; De Campos et al., 2016; Gradim et al., 2014; Pedrosa-Soares et al., 2011; Peixoto et al., 2015; Richter et al., 2016; Silva et al., 2011; Tedeschi et al., 2016). Most collisional peraluminous granites ascribed to the G2 supersuite, like the Carlos Chagas batholith, occur in the northern back-arc region to the east of the Rio Doce arc (G1 supersuite), and along the northeastern sector of the Araçuaí orogen (Figs. 1 and 2).

The Carlos Chagas batholith, extends in a N-S direction between latitudes 17°S and 19°30′S in the states of Espírito Santo, Minas Gerais and Bahia. Cropping out over an area of approximately 14,000 km^2, it is one of the largest bodies of S-type granite in the world. The first characterization and delimitation of such a large amount of S-type granite resulted from systematic geological mapping covering the whole area of the batholith (Castañeda et al., 2006; Gradim et al., 2014; Pedrosa-Soares et al., 2001, 2006, 2007; Pinto et al., 2001; Queiroga et al., 2012; Roncato, 2009; Roncato et al., 2012; Sampaio et al., 2004). These publications also characterize the CCB lithotypes, and describe their main field, petrographic, structural and lithochemical features (see below).

The typical CCB rocks are coarse-grained S-type granites rich in K-feldspar megacrysts and relatively poor in mafic minerals, the so-called Carlos Chagas leucogranite. Macroscopically, the batholith shows striking structural variations from non-deformed granites with well-preserved igneous fabrics to increasingly deformed varieties showing the regional ductile foliation (Cavalcante et al., 2013; Gradim et al., 2014; Pedrosa-Soares et al., 2011). The deformed CCB granites frequently show post-kinematic leucosomes of garnet- and cordierite-bearing leucogranite (G3) in the form of veins and patches, overprinting the regional foliation Sn (Gradim et al., 2014; Pedrosa-Soares et al., 2011). The G3 leucosomes generally show gradational contacts in relation to the host G2 granite, suggesting an autochthonous origin for the G3 melt. Locally, sharp contacts between G3 veins and the host G2 granite can occur, indicating mobility of the G3 melt (Gradim et al., 2014; Pedrosa-Soares et al., 2011; Roncato, 2009). The G3 leucogranites show many remnants of the host G2 granite, in the form of paleosome (restites) and biotite-sillimanite-rich schlieren (Pedrosa-Soares et al., 2006; Roncato, 2009). The U–Pb ages of G2 and G3 from the same outcrops (Fig. 2) show that G3 leucogranites (ca. 545–530 Ma) are 40 Ma to 50 Ma younger than the older Carlos Chagas and Ataléia granites (Gradim et al., 2014; Pedrosa-Soares et al., 2011; Silva et al., 2002, 2011).

Foliated peraluminous granites of the G2 Ataléia suite (ca. 590–570 Ma) and granulite facies paragneiss complexes (Jequitinhonha and Nova Venécia; Gradim et al., 2014; Moraes et al., 2015; Richter et al., 2016) surround and underlie the CCB, and also appear as isolated massifs in erosional windows within the batholith (Fig. 2). The contact of the CCB with its host rocks varies from intrusive to gradational, with the Nova Venécia and Jequitinhonha paragneisses, to gradational or sharp, with the Ataléia foliated granites, and is defined by shear zones in some places. However, no evidence of large displacements along the CCB contacts has been described. Regionally, the CCB is relatively poor in xenoliths of the host rocks, which tend to be more common along the batholith borders.

The batholith was intruded by a number of plutons, dikes and veins composed of granitic, charnockitic and gabbroic rocks of the post-collisional (525 Ma–490 Ma) G5 supersuite (Belém, 2014; De Campos et al., 2004, 2016; Gradim et al., 2014). G5 intrusions cut the regional and local structures of the CCB rocks, and locally imposed high-grade metamorphic recrystallization on their host rocks (Belém, 2014; De Campos et al., 2016; Pedrosa-Soares et al., 2011; Queiroga et al., 2012; Roncato et al., 2012).

Ages of magmatic crystallization from 576 ± 8 Ma to 568 ± 5 Ma (uncertainties reported as 2σ) for the CCB have been constrained by several SHRIMP and LA-ICP-MS zircon U–Pb studies (Gradim et al., 2014; Silva et al., 2002, 2011; Vauchez et al., 2007). The youngest metamorphic age (549 ± 28 Ma) from the ultramylonite, together with the age (546 ± 7 Ma) of a garnet-cordierite granite (G3) forming leucosomes that overprint a foliated Carlos Chagas leucogranite were suggested to constrain the end of the collisional stage (Gradim et al., 2014). However, Noce et al. (2004), Pedrosa-Soares et al. (2011), and Silva et al. (2002, 2011) reported ages as young as 532 ± 11 to 531 ± 10 Ma for G3 granites. To some extent, the uncertainties on some of the age data from these previous studies make the interpretations of the timing of crystallization, metamorphism and possible anatexis speculative.
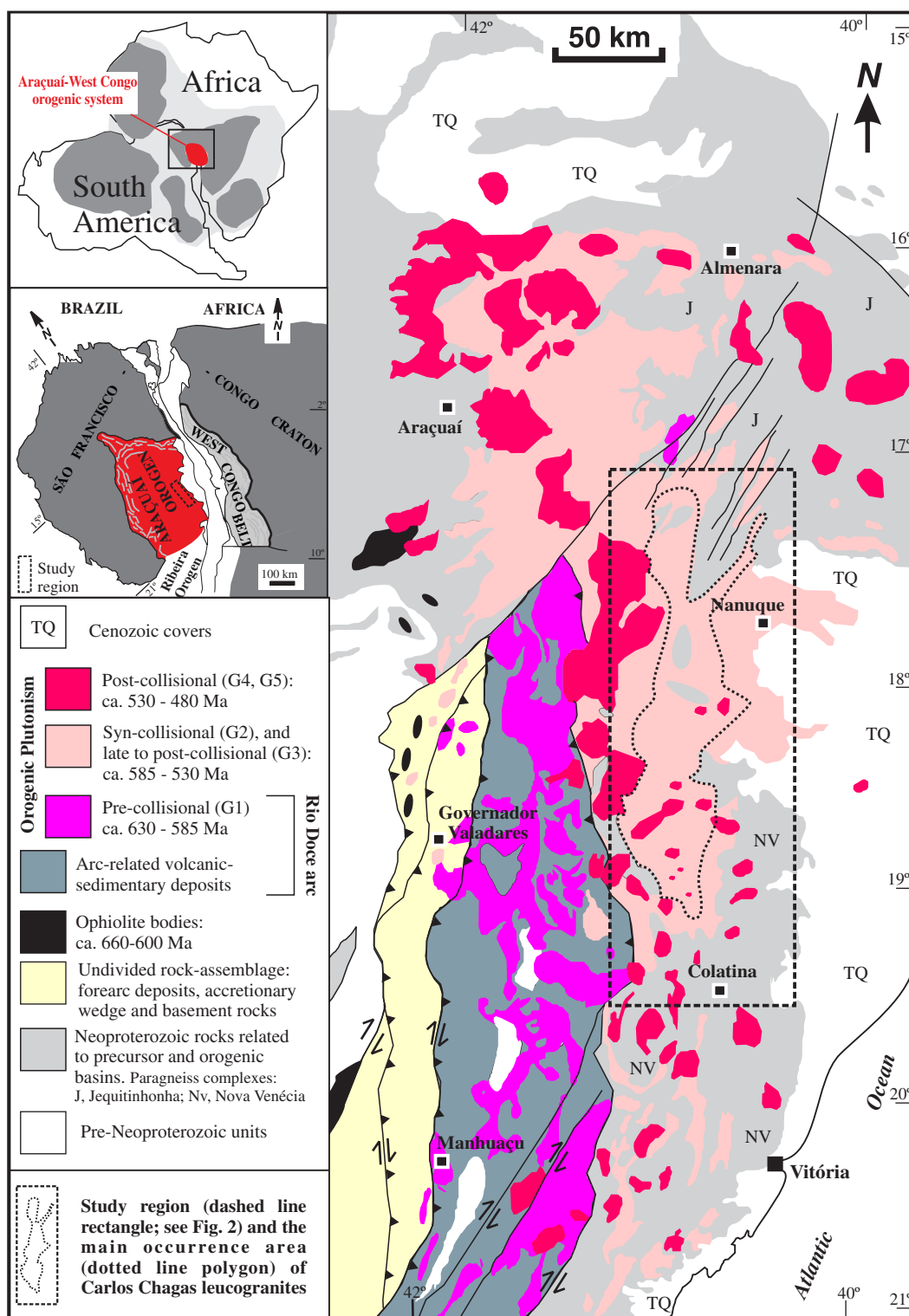
Fig. 1. Simplified geological map of the Araçuaí orogen (modified from Pedrosa-Soares et al., 2011), showing location of the study region (dashed rectangle) and the main occurrence area (dotted polygon) of the Carlos Chagas leucogranites.

3. Sampling and petrography

Representative samples were collected over an extensive area of the CCB (Fig. 2), with most samples being sourced from large dimension stone quarries and road cuts. Petrographic studies were carried out on sixty-four thin sections, including the thirty-five thin sections previously studied by Castañeda et al. (2006), Gradim et al. (2007), Queiroga

et al. (2012) and Roncato et al. (2012). Three different mineral assemblages characterize the Carlos Chagas leucogranite from the G2 supersuite (mineral abbreviation after Whitney and Evans, 2010):

Assemblage 1: Qz + Pl + Kfs + Bt + Grt + Ilm ± Rt
Assemblage 2: Qz + Pl + Kfs + Bt + Grt + Ilm + Sil
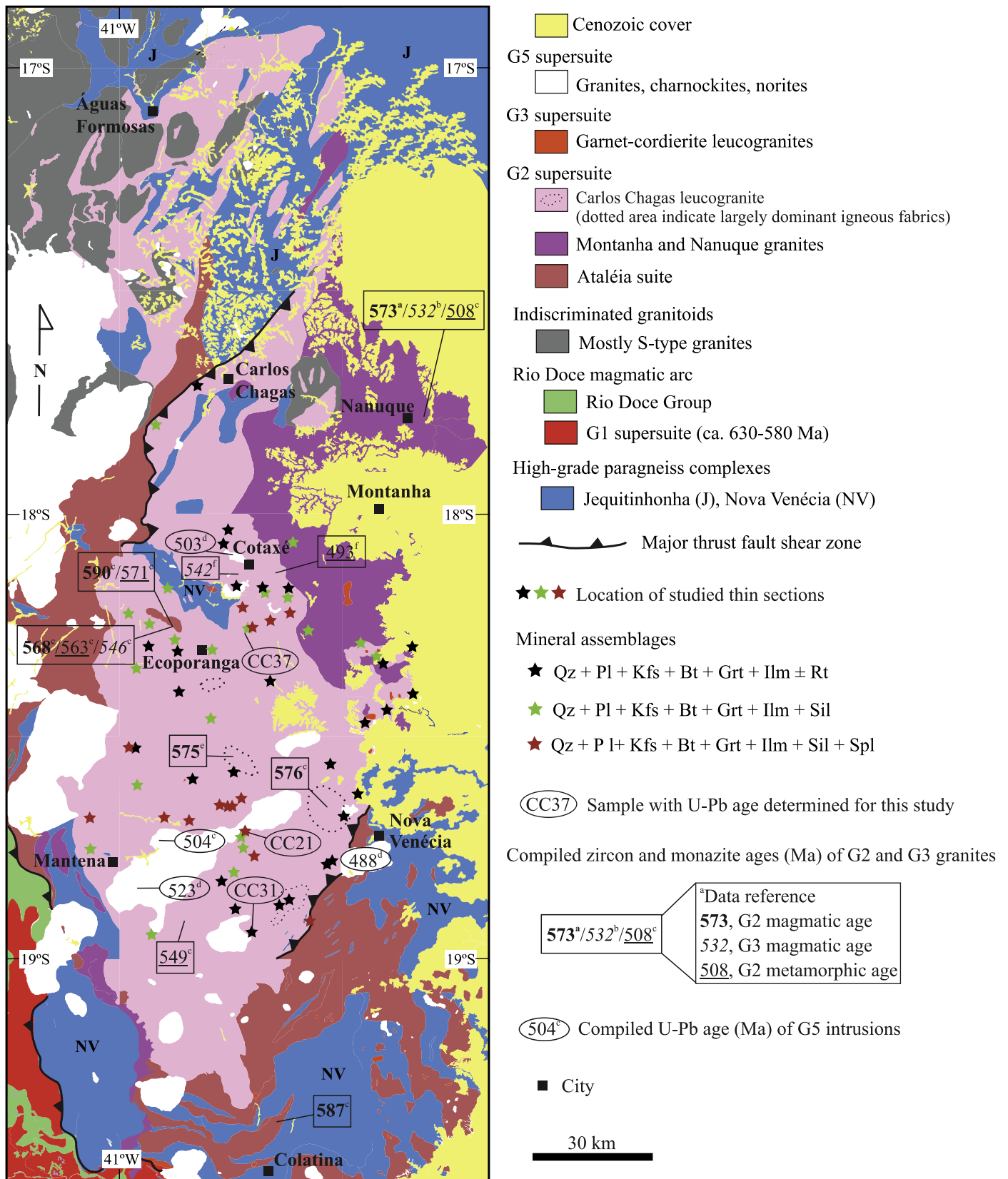Assemblage 3: Qz + Pl + Kfs + Bt + Grt + Ilm + Sil + Spl

Fig. 2. Simplified geological map for the study region (compiled from 1:100.000 scale maps published by Baltazar et al., 2010; Castañeda et al., 2006; Gradim et al., 2007; Pinto et al., 2001; Queiroga et al., 2012; Roncato et al., 2012), showing the area covered by Carlos Chagas leucogranites, location of samples (CC) analyzed in this study, and compiled U–Pb geochronological data from: a, Silva et al. (2002, 2011); b, Pedrosa-Soares et al. (2011); c, Gradim et al. (2014); d, De Campos et al. (2016); e, Vauchez et al. (2007); f, Pedrosa-Soares et al. (2006).

Table 1
Mineral modal proportions (in vol.%) based on the thin sections.

Assemblages	Qz	Pl	Kfs	Bt	Grt	Sil	Hc
1	29–45	8–15	22–43	2–5	4–18	–	–
2	22–37	15–22	17–28	1–4	3–15	1–5	–
3	25–41	17–24	28–39	0.5–3	4–10	0.5–2	<1

Scanned images of the thin sections were used in conjunction with the software programme ImageJ (Rasband, 1997–2012) to determine the modal proportions of the minerals which are presented in Table 1.

Fig. 3 shows the macroscopic features of representative rock samples from each mineral assemblage type.

3.1. Assemblage 1

The samples comprise foliated and non-foliated, very coarse- to coarse grained granites with abundant euhedral K-feldspar megacrysts (Fig. 3a,b). Many large outcrops show that the non-deformed facies with macroscopically well-preserved igneous fabrics progressively grade into the deformed facies. The mineral assemblage in both foliated and non-foliated varieties is characterized by large garnet porphyroblasts
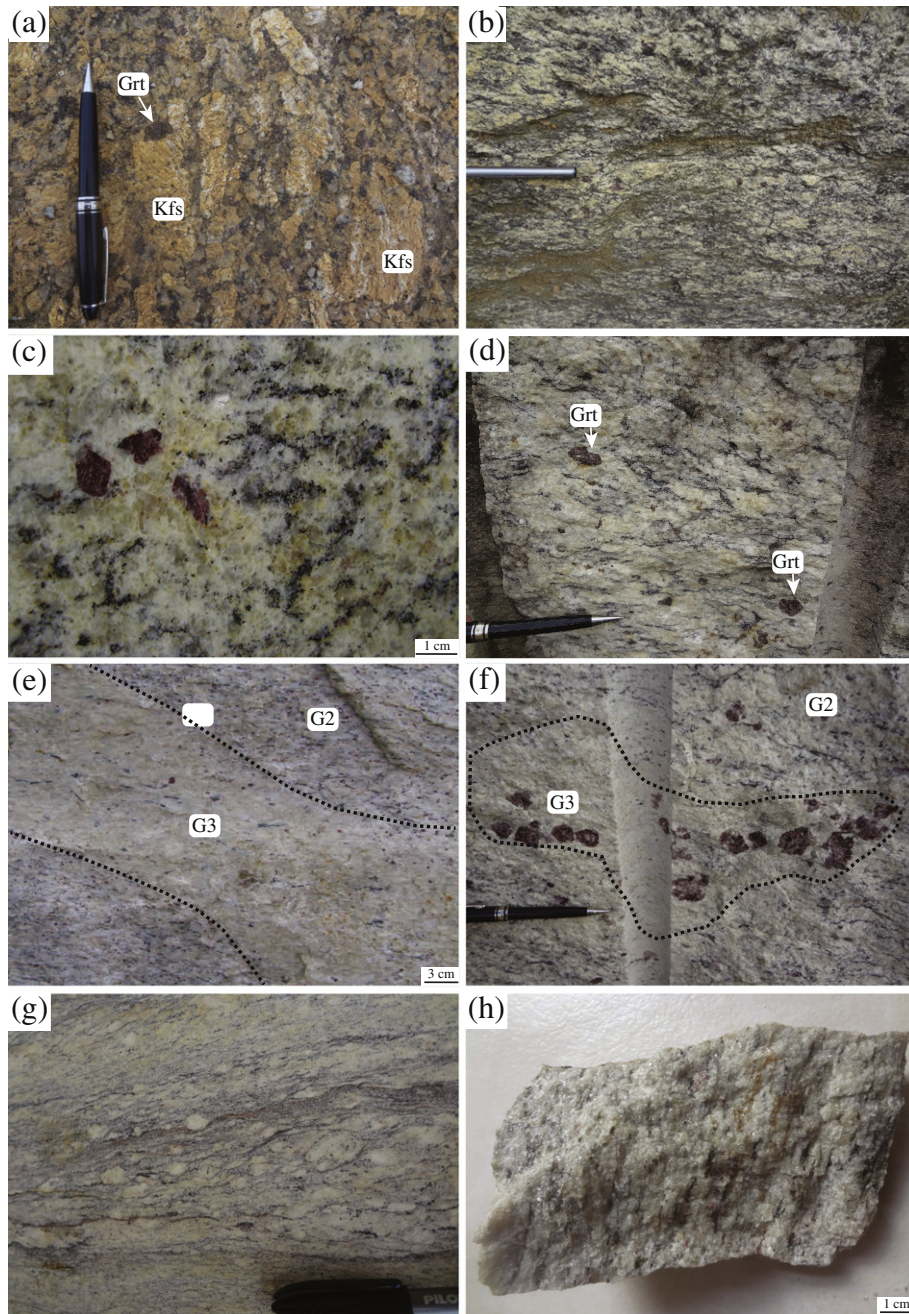

Fig. 3. Macroscopic features in rocks from mineral assemblages 1 (a,b), 2 (c–f) and 3 (g,h). Note that most examples are deformed to some degree. (a) Very coarse-grained granite showing fabrics interpreted to record a transition from magmatic deformation marked by the alignment of K-feldspar megacrysts, to solid-state recrystallization of interstitial quartz and K-feldspar. (b) Regional foliation (S_n) marked by biotite in the granite. (c) Weakly deformed leucogranite showing euhedral to subhedral garnet crystals. (d) Sigma shape of K-feldspar grains in sillimanite- and garnet-bearing leucogranite. (e) G3 leucogranite vein (dashed line) cutting the G2 granite. (f) Dashed lined delimited G3 garnet-bearing leucogranite patches. (g) Mylonite showing feldspar porphyroclasts surrounded by a quartz-rick matrix. (h) Highly deformed mylonitic leucogranite, with foliation marked by sillimanite needles, greenish spinel and quartz ribbons.

crystals in a coarse- to very coarse-grained biotite-bearing quartz-feldspathic matrix (Fig. 4a). The accessory assemblage is dominated by rutile, ilmenite, zircon, monazite and apatite, followed in abundance by sulfide phases (e.g. pyrite, chalcopyrite and sphalerite). The majority of garnet porphyroblasts (Grt$_1$, 5–35 mm) are poikiloblastic and contain numerous inclusions (40–380 μm) of rounded biotite, lobate and rounded quartz (Fig. 4b,c), as well as the accessory minerals (ilmenite, rutile, apatite, zircon and monazite). Thin films of quartz and plagioclase occur along the boundaries of garnet and euhedral rutile crystals (Fig. 4d). Additionally, thin films of quartz are also observed between plagioclase grains in the matrix (Fig. 4e).

Three textural varieties of biotite are recognized in these samples. The first type is characterized by rounded inclusions in poikiloblastic garnet, as mentioned above (Fig. 4b,c). Matrix biotite consists of small single crystals and/or clots of crystals (0.1–1.7 mm) aligned with the regional foliation (Fig. 4a,e). Zircon is a common inclusion in these biotite crystals and some grains show rims that have been partially altered to ilmenite. The last type (0.16–1.2 mm) occasionally occurs at the margins of the larger garnet crystals (Fig. 4a,c).

Plagioclase and quartz in the matrix commonly have sutured boundaries typical of grain boundary migration at high-temperature (Fig. 4f). K-feldspar occurs mainly as megacrysts in the matrix (up to 12 cm) and surrounding garnet crystals. Euhedral K-feldspar crystals are common in all but the most strongly deformed granites, presumably due to strain partitioning preferentially into the surrounding quartz-bearing matrix.

3.2. Assemblages 2 and 3

Mineral assemblages 2 and 3 are only found in the deformed Carlos Chagas leucogranite that vary progressively from foliated granites with an incipient augen structure to mylonitic granites (Fig. 3c–h). The foliation around sigmoidal porphyroclasts of K-feldspar and garnet are a result of anastomosing foliation and form augen structure. Moreover, the ductile deformation is attested by presence of quartz ribbons, recrystallization tails around (rotated or not) garnet and feldspar porphyroclasts, and mineral trails of sillimanite needles and green spinel. Generally, the biotite content decreases (from 5 vol.% to <1 vol.%) with increasing deformation. Deformed granites exhibiting the regional foliation Sn largely predominates in the Carlos Chagas batholith.

The samples differ from assemblage 1 by the presence of sillimanite in a foliation that wraps around the biotite-bearing garnet porphyroblasts (Grt$_1$) and by formation of a second generation of garnet (Grt$_2$) (Fig. 5a,b). In these samples, matrix sillimanite forms prismatic aggregates with inclusions of rounded plagioclase. In addition, corroded plagioclase occurs adjacent to sillimanite prisms. Grt$_2$ occurs as smaller euhedral/subhedral crystals (0.1–0.6 mm) with inclusions of sillimanite needles that are aligned with foliated matrix sillimanite (Fig. 5a).

Distinct textural types of biotite are also identified in assemblages 2 and 3. Matrix biotite commonly shows evidence of having formed through reactions between melt and ferromagnesian minerals in that it commonly occurs in symplectites with quartz (Fig. 5c). The
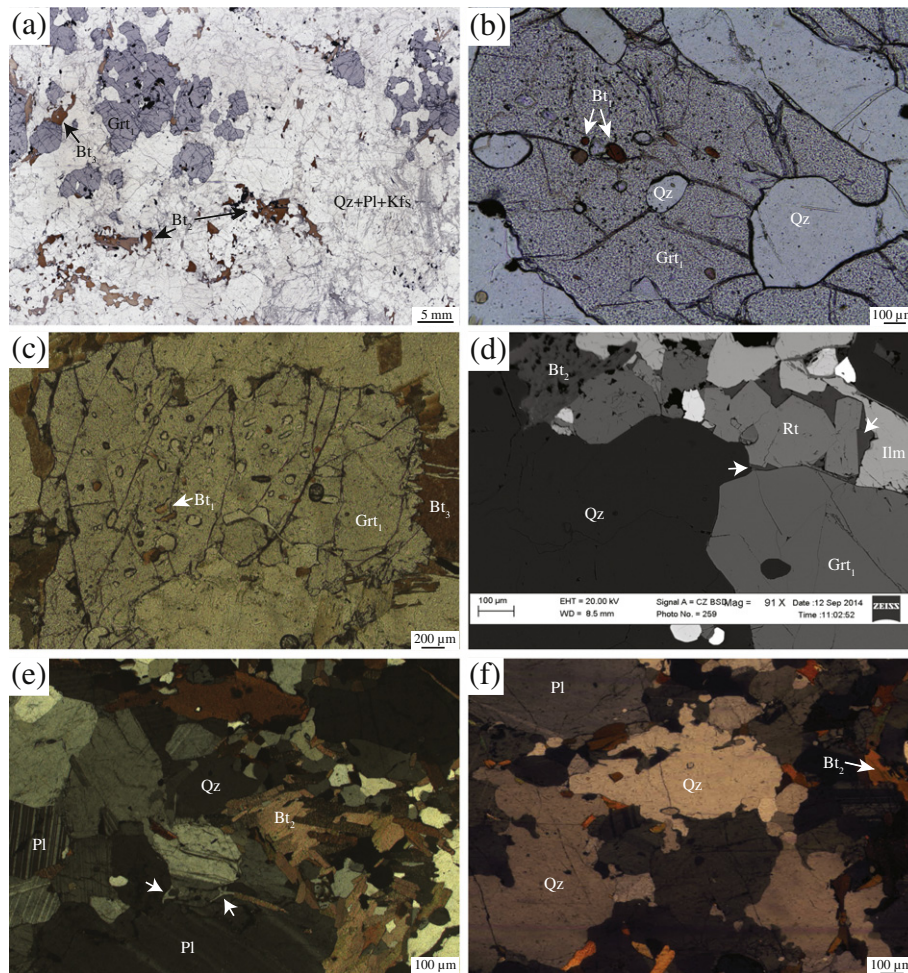

Fig. 4. Photomicrographs of microstructures in rocks from assemblage 1. (a) Scanned thin section showing garnet porphyroblasts in a biotite-bearing quartz-feldspathic matrix. (b) Garnet porphyroblasts (Grt$_1$) in the foliated granite, showing rounded biotite and quartz inclusions. (c) Multiple rounded and quartz biotite inclusions in garnet, which are likely to be the consequence of a biotite melting reaction. (d) BSE image showing thin films of plagioclase (white arrows) along garnet boundaries and surrounding euhedral rutile crystals. (e) Quartz films (white arrows) between plagioclase grains in matrix. Foliation marked by biotite. (f) Sutured boundaries in quartz formed by grain-boundary bulging.
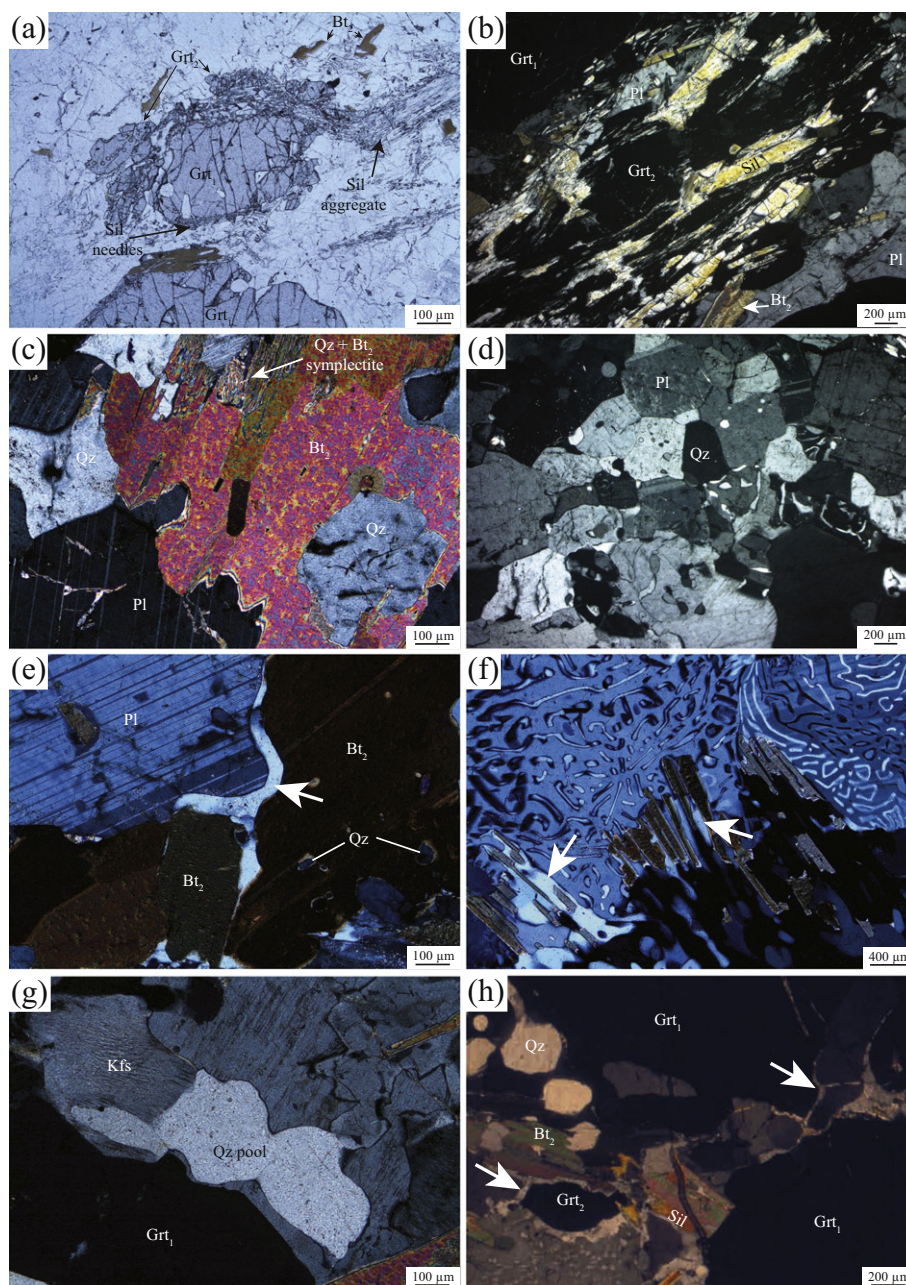
Fig. 5. Photomicrographs of microstructures observed in rocks from assemblages 2 and 3. (a) Two different textural varieties of garnet and their relationships with the biotite-sillimanite fabric. Mineral inclusion suites in both garnet generations are consistent with their production as peritectic products of incongruent melting reactions, which consumed biotite. Sillimanite needles wrap around Grt_1, but are overgrown by Grt_2. (b) An aggregate of garnet crystals (Grt_2) which overprint the biotite-sillimanite foliation. (c) Quartz and biotite symplectite in the matrix. (d) Development of polygonal grains in the quartzofeldspathic matrix. (e) Cuspate quartz (white arrow) along the grain boundaries of biotite and plagioclase in the matrix. (f) Quartz-filled melt pools (white arrow) around biotite grains. Intergrowth myrmekite. (g) Quartz-filled melt pools adjacent to garnet. (h) Films of quartz (white arrow) in garnet boundaries.

quartzofeldspathic matrix generally shows evidence for high temperature intracrystalline deformation and recrystallization, such as undulose extinction and development of subgrains in quartz, irregular twinning in plagioclase and polygonal grains of quartz and plagioclase (Fig. 5d). Intergrowths of myrmekite and albite in K-feldspar are common. Plagioclase and quartz with cuspate-lobate shapes occur as interstitial phases (Fig. 5e). Quartz-filled former melt pools are observed adjacent to garnet and biotite (Fig. 5f,g). Pseudomorphed thin melt films commonly occur surrounding both generations of garnet crystals (Fig. 5h).

In contrast to assemblage 2, the assemblage 3 shows spinel as dark-green, elongated, subhedral to rounded grains typically surrounded garnet and occasionally included in sillimanite and garnet.

4. Mineral chemistry

The mineral chemistry of garnet, biotite, plagioclase, K-feldspar, spinel and ilmenite is listed in Supplementary data (Table 1); the analytical methodology is reported in Supplementary material. The end-member concentrations were calculated as: $X_{Alm} = Fe^{2+}/(Fe^{2+}+Mg + Mn + Ca)$, $X_{Py} = Mg/(Fe^{2+}+Mg + Mn + Ca)$, $X_{Spss} = Mn/(Fe^{2+}+Mg + Mn + Ca)$, $X_{Grs} = Ca/(Fe^{2+}+Mg + Mn + Ca)$, $Mg\# = Mg/(Mg + Fe^{2+})$, $X_{An} = Ca/(Ca + Na + K)$, $X_{Ab} = Na/(Ca + Na + K)$, $X_{Or} = K/(Ca + Na + K)$ and $X_{Ghn} = Zn/(Zn + Mg + Fe^{2+})$. Fe^{3+} concentration in garnet, ilmenite and spinel was calculated using the general equation of Droop (1987).
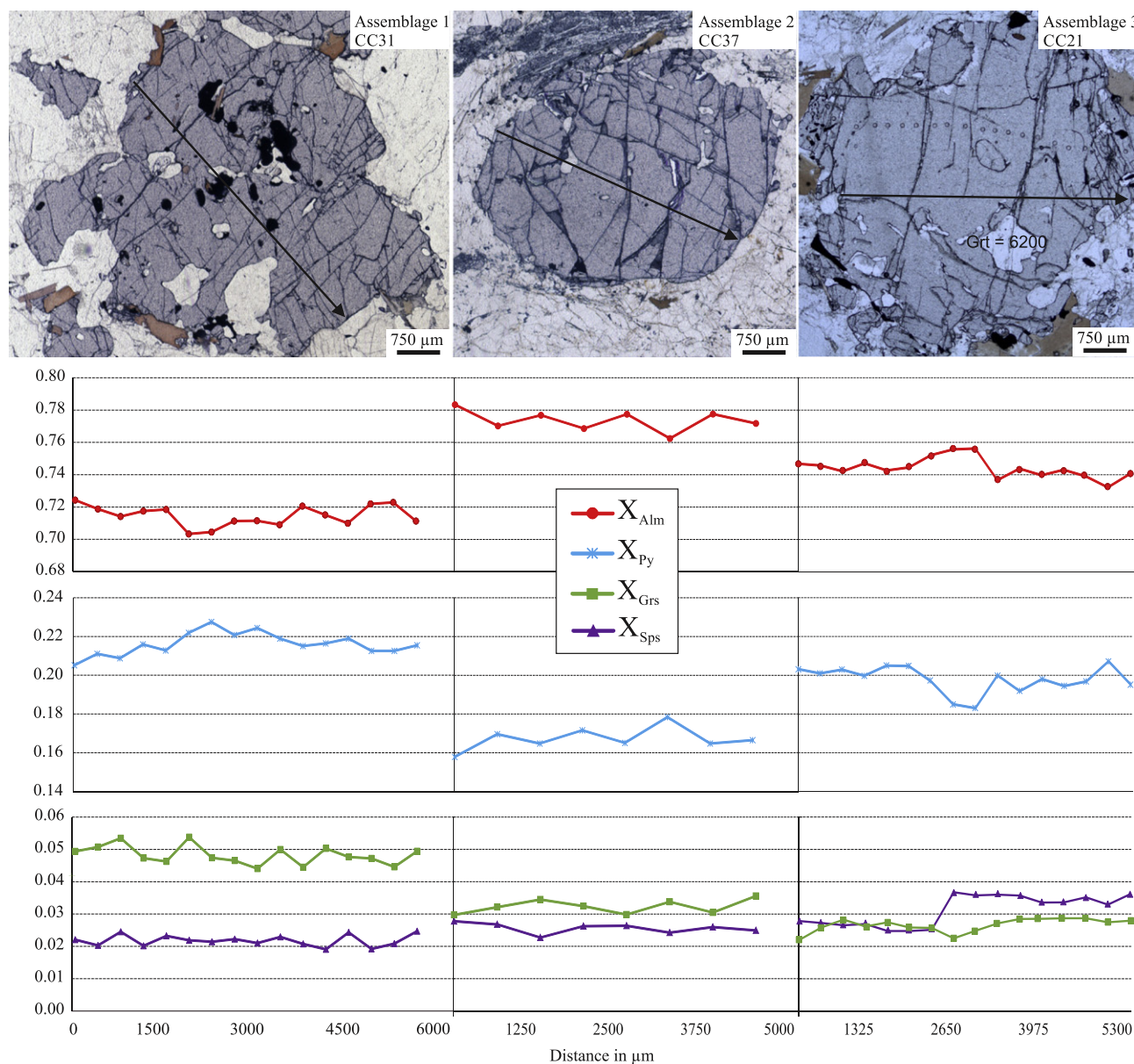
Fig. 6. Compositional profile of representative poikiloblastic garnet (Grt_1) analyzed in each mineral assemblage.

Both generations of garnet are almandine-rich with subordinate pyrope, and minor grossular and spessartine. Individual crystals do not display any significant major element zonation (Figs. 6 and 7a, see more details in Supplementary data – Table 1). The Grt_1 crystals have X_{Alm} and X_{Py} ranging of 0.70 to 0.79 and 0.15 to 0.23, respectively (Figs. 6 and 7a). X_{Grs} is higher in Grt_1 from assemblage 1 (X_{Grs} = 0.04–0.06) than Grt_1 from assemblages 2 and 3 (X_{Grs} ~ 0.03) (Figs. 6 and 7a). Spessartine component in Grt_1 is similar in all assemblages (X_{Spss} = 0.02–0.03) and Mg# varies between 0.16 and 0.25. Grt_2 is characterized by slightly different compositions to Grt_1, which is indicated by an increase in Fe-content (X_{Alm} = 0.78–0.82) and decrease in Mg-content (X_{Py} = 0.12–0.17) (Fig. 7a). For Grt_2, its Mg# varies between 0.13 and 0.18. Spessartine and grossular contents are homogeneous in the Grt_2 crystals (X_{Spss} ~ 0.03 and X_{Grs} ~ 0.02).

As shown in Fig. 7b, biotite displays variable composition depending on its microstructural position. Biotite inclusions in Grt_1 present high Ti (0.48–0.74) and Mg# (0.50–0.69) values compared to matrix biotite (Ti = 0.39–0.63 and Mg# = 0.40–0.52). Retrograde biotite around garnet is characterized by low Ti and intermediate Mg# values (Ti = 0.25–0.58 and Mg# = 0.48–0.59).

Matrix plagioclase is unzoned and displays X_{An} values of 0.22–0.33 (Supplementary data – Table 1). Plagioclase adjacent to garnet has the same composition as the matrix crystals, whereas inclusions in garnet have X_{An} values ranging from 0.25 to 0.29, and inclusions in sillimanite have X_{An} of ~0.26. Matrix K-feldspar has X_{Or} values of 0.71 to 0.92. Spinel crystals have relatively high Zn-content with X_{Ghn} of 0.10–0.20.

5. Rare earth element composition of garnet

Rare earth element (REE) concentrations in garnet were measured by LA-ICP-MS (Supplementary data - Table 2, see methodology in Supplementary material) from the same three thin sections representing assemblages 1, 2 and 3 from which major element compositions were reported.

The Grt_1 crystals from all assemblages are enriched in HREE, with ΣGd-Lu of 86–467 ppm. They have lower Gd_N/Lu_N ratios in the rim (0.21–2.91) than in the cores (0.08–0.42) (Fig. 8). If the small number of samples studied can be considered to be representative, the garnet rims also display a larger negative Eu anomaly in assemblages 2 and 3 (Eu/Eu* = 0.01–0.02) than the assemblage 1
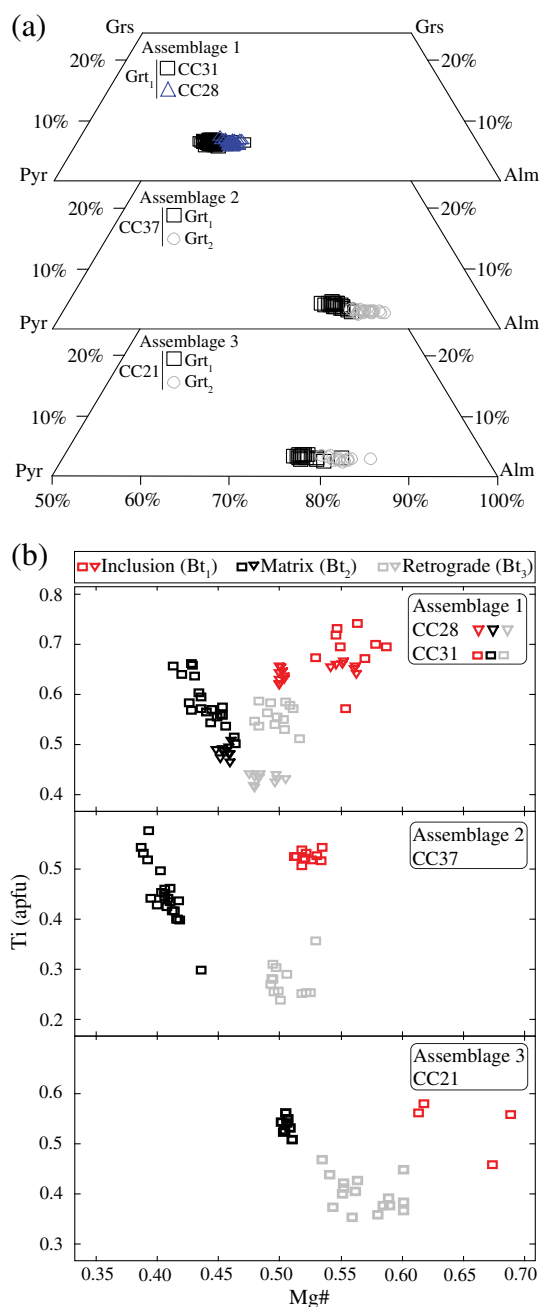
Fig. 7. Mineral chemistry for all mineral assemblages from CCB. (a) Grs-Alm-Py garnet diagram. (b) Biotite compositions plotted on a Ti (apfu) v. Mg#.

Fig. 8. Chondrite-normalized (McDonough and Sun, 1995) REE patterns in garnet from Carlos Chagas leucogranite. (a) Grt$_1$ from assemblage 1 are enriched in HREE, have flat HREE patterns and negative Eu anomalies. (b) Grt$_1$ are richer in Gd-Dy than Grt$_2$ from assemblage 2. (c) Both garnet generations from assemblage 3 display flat HREE patterns and pronounced negative Eu anomalies.

rocks (Eu/Eu* = 0.04–0.07) (Fig. 8). The Grt$_2$ crystals have ΣGd-Lu of 175–290 ppm that is within the range of Grt$_1$. In assemblage 2, both the cores and rims vary from slightly positive to slightly negative HREE ratios (Gd$_N$/Lu$_N$ = 0.69–1.60) (Fig. 8b). Grt$_2$ crystals from assemblage 3 have slightly positive slope HREE patterns (Gd$_N$/Lu$_N$ = 0.51–0.71, Fig. 8c). Both samples show broadly similar negative Eu anomalies (Eu/Eu* = 0.01) (Fig. 8b,c).

6. P–T conditions

Phase equilibrium modeling was performed in the chemical system NCKFMASHTO (Na$_2$O-CaO-K$_2$O-FeO-MgO-Al$_2$O$_3$-SiO$_2$-H$_2$O-TiO$_2$-Fe$_2$O$_3$) using Theriak-Domino software (De Capitani and Petrakakis, 2010), in combination with the updated tc2td.exe converted Holland and Powell (1998) database created by Tinkham. The modeling used the
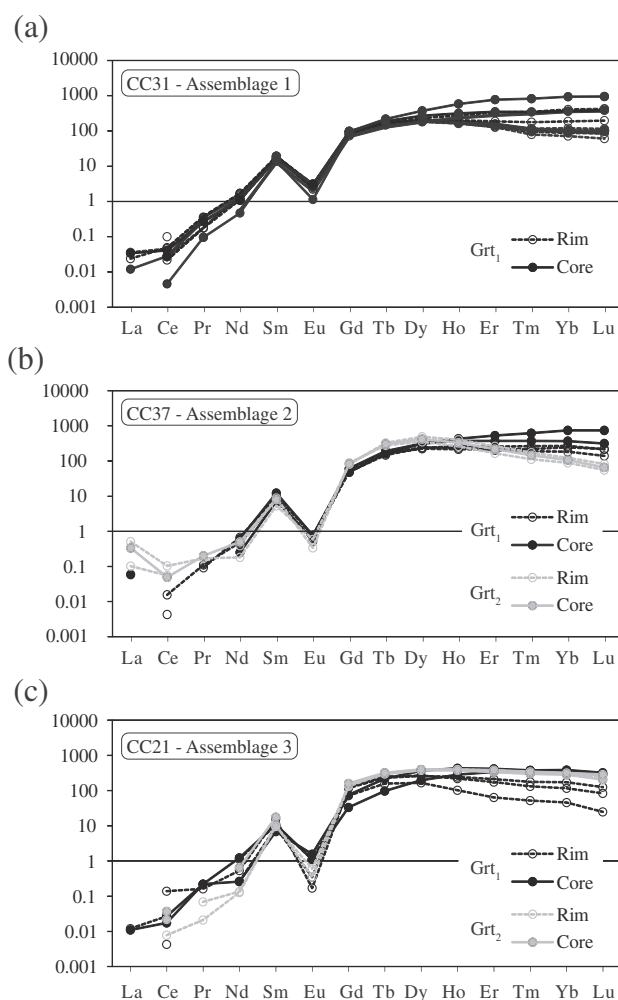
a-x relationships of White et al. (2007) for silicate melt, garnet and biotite; White et al. (2002) for orthopyroxene and spinel; White et al. (2000) for ilmenite; Coggon and Holland (2002) for white mica; and Holland and Powell (2003) for plagioclase and alkali feldspar. Pseudosections were calculated using the bulk composition from foliated Grt-bearing (samples CC28 and CC31 – assemblage 1) and Sil-Grt-bearing granites (sample CC37 – assemblage 2) (Table 2). Phase equilibrium modeling could not be successfully conducted for the Spl-Sil-Grt-bearing samples (assemblage 3) because the available a-x models for spinel do not include Zn and the Zn content of the spinel in these samples is too high to be ignored (7.20 wt.% - Supplementary data – Table 1). CCB rocks record textural and mineral chemical evidence of partial melting (Figs. 4d,e and 5c,e,f,g,h). In addition, the peritectic garnet produced by partial melting is well preserved, which necessitates substantial melt loss prior to cooling (White and Powell, 2002). Consequently, the prograde evolution of the CCB cannot be constrained by phase equilibrium modeling in these melt-depleted bulk compositions (White and Powell, 2002). However, the unretrogressed nature of the rocks does allow for detailed investigation peak metamorphic conditions recorded by assemblage 1 and 2.

Appropriate values for water content were investigated on T-X pseudosections and the bulk H$_2$O values were chosen according to the methodology of White et al. (2001), such that the solidus was located just below the lowest temperature of occurrence of the interpreted

Table 2
Bulk composition used for metamorphic modeling and normalized to 100%. H_2O and Fe_2O_3 content.

Samples	SiO$_2$	Al$_2$O$_3$	TiO$_2$	FeO	Fe$_2$O$_3$	MgO	CaO	Na$_2$O	K$_2$O	H$_2$O	Total
CC28	74.57	12.78	0.38	2.69	0.03	0.59	1.08	2.16	5.50	0.22	100.00
CC31	66.81	15.82	1.06	5.33	0.15	1.32	2.00	2.82	4.40	0.29	100.00
CC37	60.69	24.44	0.22	9.03	0.00	0.90	1.47	2.51	0.61	0.12	100.00

peak assemblage (CC28 = 0.22%, CC31 = 0.28% and CC37 = 0.12%). The Fe_2O_3 content for all compositions were determined using P-X pseudosections with T fixed at 800 °C (CC28 and CC31) and 760 °C (CC37). This is consistent with experimental studies which document that these are the approximate minimum temperatures for garnet formation by absent-fluid melting reactions consuming biotite, quartz and plagioclase, and biotite, sillimanite, quartz and plagioclase, respectively (e.g. Castro et al., 1999; Patiño Douce and Harris, 1998; Patiño Douce and Johnston, 1991; Pickering and Johnston, 1998; Stevens et al., 1997). The value chosen for Fe^{3+} concentration in each bulk composition results in modeled Fe^{3+} concentrations in ilmenite and garnet, within the field of the relevant peak assemblage, that are in agreement with measured values in these minerals in the specific sample.

6.1. Assemblage 1

Five samples were modeled to evaluate the P–T conditions of the assemblage 1 (Pl + Kfs + Grt + Bt + Qz + Rt + Ilm + melt). The modeling of two representative samples is presented below (samples CC28 and CC31). The results from another three samples are presented in Supplementary material (Figure SM1), indicating that the assemblage 1 is stable between 770 and 900 °C and 9.5–13 kbar.

6.1.1. Sample CC28

In this sample, the assemblage 1 is stable between 780 and 860 °C and 9.2–12.6 kbar (Fig. 9a), with a melt fraction <5 vol.% (Fig. 9b). Within this field, the amount of garnet (3–6 vol.%) and biotite (<3 vol.%) (Fig. 9c,e) is consistent with the quantities estimated in thin section (~4% and ~2%, respectively). The modeling shows an increase in the mode of Grt, melt and rutile, coupled with a decrease in the mode of Bt as temperature increases over the range defined by the peak assemblage (Fig. 9c,e). This is consistent with the occurrence of fluid-absent melting reactions consuming biotite.

Modeled garnet composition shows Mg# of 0.19–0.30, X_{Grs} of 0.04–0.10 and X_{Alm} of 0.64–0.77 in the peak assemblage field (Fig. 9c,d). These values encompass those of measured in Grt$_1$, showing Mg#, X_{Grs} and X_{Alm} values of 0.20–0.22, 0.04–0.06 and 0.72–0.74, respectively (Supplementary data - Table 1). Mg# values for the modeled biotite range from 0.46 to 0.61 in the peak field (Fig. 9e) and measured values for biotite inclusions (Bt$_1$) in garnet range from 0.50 to 0.56 (Supplementary data - Table 1). The use of X_{Grs}, X_{Alm}, Grt Mg# and Bt$_1$ Mg# values help to more tightly constrain the P–T conditions of the peak assemblage to 790–820 °C and 9.5–10.5 kbar (Fig. 9f).

6.1.2. Sample CC31

The peak assemblage Pl + Kfs + Grt + Bt + Qz + Rt + Ilm + melt occurs at P–T conditions between 800 and 870 °C and 8.9–13.4 kbar (Fig. 10a). Within this field the maximum amount of melt is <6 vol.% (Fig. 10b). This is consistent with the mineral assemblage observed in the assemblage 1 rocks that commonly show ilmenite and rutile as inclusions in Grt$_1$ and also associated pseudomorphed thin films of melt along the garnet boundaries (Fig. 4d). In the peak assemblage field, the garnet mode ranges from 8 to 13 vol.% (Fig. 10c), while biotite is <5 vol.% (Fig. 10e). These modes are consistent with the garnet

and biotite proportions estimated in thin section (~12% and ~4.5%, respectively) and outcrop (5–10% and 1–4%, respectively).

Modeled garnet and biotite compositions record Mg# of 0.23–0.35 (Fig. 10c) and 0.54–0.64 (Fig. 10e) in the assemblage field, respectively. The values of Mg# number measured in Grt$_1$ range from 0.21 to 0.25, while the biotite inclusions in garnet have values of 0.55–0.59 (Supplementary data - Table 1). Within the peak assemblage field, the garnet and melt proportions increase with increasing temperature while biotite proportion decreases (Fig. 10b,c,e), consistent with biotite-breakdown via incongruent melting reactions. X_{Grs} and X_{Alm} values are increased by increasing pressure and temperature, respectively. Measured Grt$_1$ composition yield X_{Grs} and X_{Alm} values that range from 0.04–0.05 and 0.70–0.72, respectively (Fig. 10d). P–T conditions of equilibration are further constrained by compositional isopleths of X_{Grs}, X_{Alm}, Grt Mg# and Bt$_1$ Mg# at 800–820 °C and 10–11 kbar (Fig. 10f).

6.2. Assemblage 2

Small domains of the garnet and sillimanite-bearing assemblage in the thin section CC37 are potentially useful to constrain the peak metamorphic conditions of the second metamorphic event. Rastered electron beam analyses of these areas were used to constrain the new bulk composition relevant to formation of the second generation of garnet. An average of the compositions of ten ~0.1 cm^2 size areas dominated by this assemblage is presented in Table 2. Using this bulk composition, the assemblage Pl + Kfs + Grt + Bt + Ilm + Qz + Sil + melt is stable between 755 and 770 °C and 4.8–9.0 kbar (Fig. 11a). In this field the amount of melt is below 3 vol.% (Fig. 11b); garnet between 16 and 17 vol.% and biotite below 2 vol.% (Fig. 11c,d). This is consistent with the mineral proportions estimated in this area of the thin section (garnet: ~17 vol.% and biotite: <1 vol.%). The lower pressure limit of the assemblage is bounded by the stability of cordierite at 5 kbar (Fig. 11a).

In the peak assemblage field, the modeled Mg# number and X_{Grs} for garnet are 0.14–0.15 and 0.01–0.04 (Fig. 11c,d), respectively. The values measured in Grt$_2$ are Mg # = 0.13–0.16 and X_{Grs} ~ 0.02 (Supplementary data - Table 1). The use of Grt Mg# and X_{Grs} isopleths allow the estimate of PT conditions of equilibration to be further constrained to approximately 770 °C and 6.6 kbar (Fig. 11e).

6.3. Melt production

As mentioned above, the excellent preservation of the garnet crystals within the metamorphosed CCB rocks necessitates significant melt loss prior to the cooling (White and Powell, 2002). To constrain the amount of melt produced in the CCB during the metamorphic events, we performed melt reintegration on samples CC31 and CC37 following the methodology of White et al. (2004).

The pseudosection modeling of the melt-reintegrated bulk composition (CC31) indicates that muscovite is stable over a substantial PT range in the protolith. During prograde metamorphism the rock underwent muscovite breakdown at ~650 °C producing 8 vol.% of melt, followed by biotite melting at 780–800 °C (Fig. 12a), with the

Fig. 9. P–T pseudosection calculated using the bulk composition from sample CC28 (assemblage 1). (a) P–T fields of peak assemblage Pl-Kfs-Grt-Bt-Ilm-Qz-Rt-Liq (bold line). (b) Plots of melt vol.%. (c) Plots of Grt Mg# and Grt vol.%. (d) Plots of X_{Grs} and X_{Alm}. (e) Plots of Bt Mg# and Bt vol.%. (f) P–T conditions of equilibrium based on the use of overlapping ranges of phase composition and abundance.
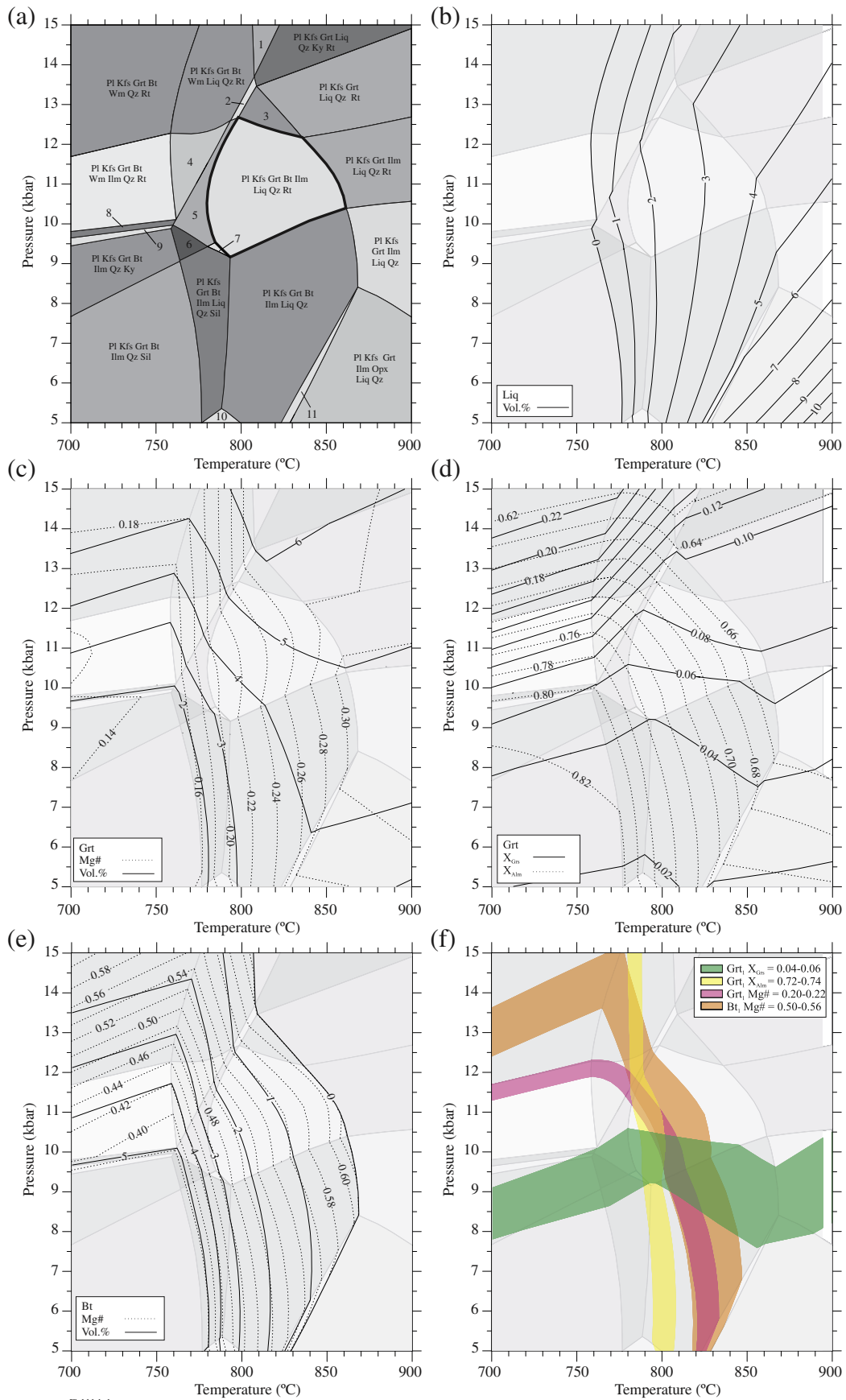
Field labels:

1 - Pl Kfs Grt Wm Liq Qz Rt, 2 - Pl Kfs Grt Bt Liq Ky Qz Rt, 3 - Pl Kfs Grt Bt Liq Qz Rt, 4 - Pl Kfs Grt Bt Wm Ilm Liq Qz Rt, 5 - Pl Kfs Grt Bt Ilm Liq Qz Ky Rt, 6 - Pl Kfs Grt Bt Ilm Liq Qz Ky, 7 - Pl Kfs Grt Bt Ilm Liq Qz Sil Rt, 8 - Pl Kfs Grt Bt Wm Ilm Qz Ky Rt, 9 - Pl Kfs Grt Bt Wm Ilm Qz Ky, 10 - Pl Kfs Grt Bt Ilm Cdr Liq Qz and 11 - Pl Kfs Grt Bt Ilm Opx Liq Qz
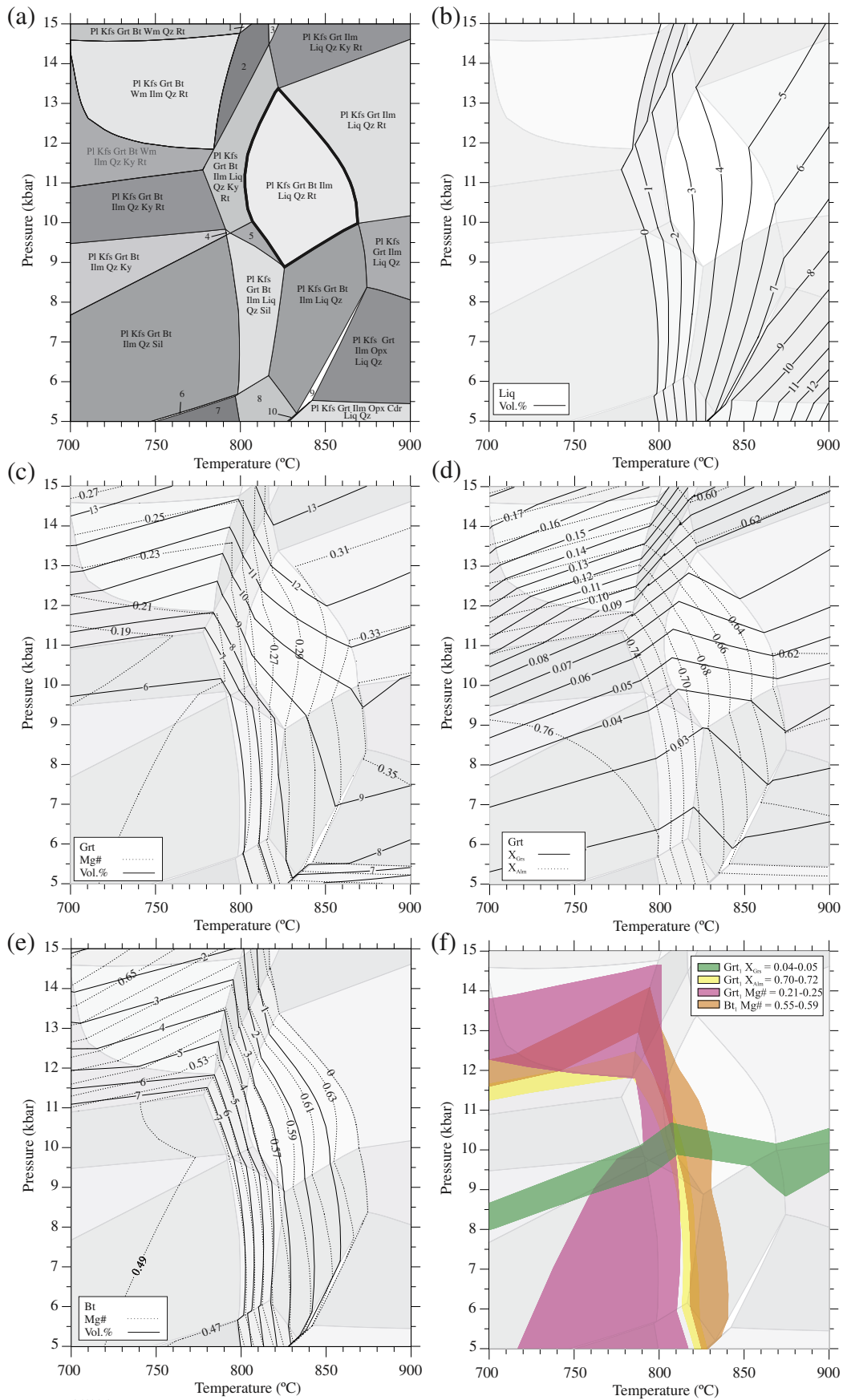
Field labels:

1 - Pl Kfs Grt Bt Wm Liq Qz Rt, 2 - Kfs Grt Bt Wm Ilm Liq Qz Rt, 3 - Kfs Grt Bt Wm Ilm Liq Qz Ky Rt, 4 - Pl Kfs Grt Bt Ilm Liq Qz Ky, 5 - Pl Kfs Grt Bt Ilm Liq Qz Sil Rt, 6 - Pl Kfs Grt Bt Ilm Cdr Qz Sil, 7 - Pl Kfs Grt Bt Ilm Cdr Qz, 8 - Pl Kfs Grt Bt Ilm Cdr Liq Qz, 9 - Pl Kfs Grt Bt Ilm Opx Liq Qz and 10 - Pl Kfs Grt Bt Ilm Opx Cdr Liq Qz

addition of 26 vol.% of melt (Fig. 12b). Under the peak metamorphic conditions (bold line in Fig. 12a), peritectic phases (garnet and rutile) and melt are produced by fluid-absent melting reactions (Bt + Pl + Qz = Grt + Rt ± Kfs + melt). The pseudosection modeling predicts that 12–34 vol.% of melt was produced as the rock progressed to the peak conditions through partial melting reactions consuming biotite.

Applying the same approach to sample CC37, muscovite and sillimanite were present just below the wet solidus in the pre-melting assemblage (Pl + Bt + Wm + Qz + Sil + H_2O) at 650 ± 20 °C and 5 ± 1 kbar (Fig. 12a). During prograde metamorphism, garnet and melt were produced by incongruent melting of biotite and sillimanite via reaction Bt + Sil + Qz + Pl = Grt + melt, as indicated by increase in mode of garnet and melt (Fig. 12b). The modeling indicates that 16–30 vol.% of melt was produced on the evolution to peak metamorphism conditions via absent-fluid melting reactions.

7. LA-ICP-MS monazite geochronology

To better constrain the timing of the two partial melting episodes that have affected the CCB, we selected a separate thin section representing each of the three assemblages from the CCB for in situ LA-ICP-MS dating of monazite. Monazite grains in the samples commonly occur as: a) inclusions in Grt_1 crystals; b) adjacent to garnet boundaries; c) within the quartzo-feldspathic matrix; d) rarely as inclusions within Grt_2 crystals. The results of all monazite analyses are presented in Supplementary data (Table 3) and the analytical methods are described in Supplementary material. Spot analyses that were more than 5% discordant were discarded in the calculation of weighted mean $^{206}Pb/^{238}U$ ages. A summary with the monazite ages is presented in Table 3.

7.1. Sample CC31 – assemblage 1

Monazite grains are euhedral to subhedral, elongated and subrounded, and are 70–190 μm in diameter. Backscattered electron (BSE) imaging displays unzoned internal structure to weakly zoned grains (Fig. 13a).

Two spot analyses of monazite included in a Grt_1 core have Th/U values of 83–85 and show a mean $^{206}Pb/^{238}U$ age of 617 ± 12 Ma (95% conf., MSWD = 0.54). Six additional spot analyses on monazite included in Grt_1, which have Th/U values of 40–134, show a mean $^{206}Pb/^{238}U$ age of 560 ± 9 Ma (95% conf., MSWD = 1.8). One spot analysis in a monazite crystal that occur along microcracks in the Grt_1 core yields a younger $^{206}Pb/^{238}U$ age of 519 ± 14 Ma (Th/U = 20). This age is within error of the age of monazite included in the rim of Grt_1 crystals ($^{206}Pb/^{238}U$ = 521 ± 14 Ma, Th/U = 27), which also displays fractures.

Matrix monazite spot analyses range from 612 to 485 Ma. Two spot analyses in the core of matrix grains, with Th/U values of 60–61, have a mean $^{206}Pb/^{238}U$ age of 562 ± 11 Ma (95% conf., MSWD = 0.68) and other spots show a concordant age of 612 ± 17 Ma and a Th/U value of 98. Four spot analyses in the rims of matrix grains, with Th/U values between 36 and 43, display a mean $^{206}Pb/^{238}U$ age of 492 ± 16 Ma (95% conf., MSWD = 2.2).

7.2. Sample CC37 – assemblage 2

Monazite occurs as euhedral to subhedral, elongated, subrounded to oval-shaped grains of 50–90 μm of diameter. BSE imaging revealed that most grains are unzoned and a few crystals display a fine brighter rim (Fig. 13b).

Four spot analyses in monazite included within Grt_1 core, with Th/U values of 9–18, generate a mean $^{206}Pb/^{238}U$ age of 557 ± 7 Ma (95%

conf., MSWD = 1.03). Two spot analyses on monazite included within the rim of Grt_1 crystals show $^{206}Pb/^{238}U$ ages of 569 ± 14 and 528 ± 14 (Th/U = 13 and 15, respectively). Eight spot analyses from matrix monazite, with Th/U values between 8 and 21, produced a mean $^{206}Pb/^{238}U$ age of 558 ± 10 Ma (95% conf., MSWD = 2.5). One spot analysis presents younger $^{206}Pb/^{238}U$ age of 484 ± 13 Ma, with Th/U value of 8.

7.3. Sample CC21 – assemblage 3

Monazite occurs in many grain shapes that vary from euhedral/subhedral, rounded/subrounded to oval, ranging from 30 to 120 μm in size. BSE images display unzoned grains as well as complex, patchy zonation in some examples (Fig. 13c).

Two spot analyses on monazite cores within the cores of Grt_1 crystals show $^{206}Pb/^{238}U$ ages of 566 ± 16 and 552 ± 15, with Th/U values of 81 and 24, respectively. Two spot analysis in monazite rims that occur along microcracks in the Grt_1 core display younger ages of 535 ± 14 (Th/U = 42) and 516 ± 14 Ma (Th/U = 15). One spot analysis on a monazite included in a Grt_2 core shows age of 515 ± 14 Ma and Th/U value of 10.

Eight spot analyses on matrix monazite, with Th/U values between 18 and 117, display a mean $^{206}Pb/^{238}U$ age of 562 ± 5 Ma (95% conf., MSWD = 1.11). Two spot analyses on matrix monazite have Th/U values of 5–25 and show a mean $^{206}Pb/^{238}U$ age of 485 ± 9 Ma (95% conf., MSWD = 0.098). One spot analysis shows an intermediate $^{206}Pb/^{238}U$ age of 527 ± 14 Ma (95% of concordance, Th/U = 20).

8. LA-ICP-MS zircon geochronology

U–Pb zircon dating can be used in combination with monazite geochronology to constrain the metamorphic history from CCB. The samples CC31 and CC21 were chosen for in situ LA-ICP-MS dating of zircon due to the common presence of zircon within and in close proximity to garnet. In addition a zircon separate was extracted from sample CC37 to investigate possible inheritance and constrain the timing of crystallization and metamorphism. The results of all zircon analyses are reported in Supplementary Data (Table 4) and the analytical methods are described in Supplementary material. Spot analyses that were more than 5% discordant were excluded from the calculation of the mean $^{206}Pb/^{238}U$ ages. A summary with the zircon ages is presented in Table 3.

8.1. Sample CC31 – assemblage 1

This sample contains 80–400 μm, prismatic, subhedral/euhedral to subrounded shaped zircon grains. Cathodoluminescence (CL) imaging displays different internal structures such as concentric and convolute zoning and some grains show isometric intergrowth (Fig. 14a).

Zircon grains included within a Grt_1 core display convolute zoning (Fig. 14a), typical of high-grade metamorphic zircon (e.g., Vavra et al., 1999). Two spot analyses, with Th/U values of 1.3–1.5, show a mean $^{206}Pb/^{238}U$ age of 563 ± 9 Ma (95% conf., MSWD = 0.094). Two spot analyses on zircon included in the rim of the same garnet crystal have Th/U values of 0.2–1.3 and yielded a mean $^{206}Pb/^{238}U$ age of 543 ± 9 Ma (95% conf., MSWD = 0.21).

We distinguished three different types of zircon in the matrix. The first variety displays magmatic oscillatory zoning in CL and is characterized by a high Th/U ratio (0.88–1.29). Four spot analyses in these domains generated a mean $^{206}Pb/^{238}U$ age of 577 ± 6 Ma (95% conf., MSWD = 0.105). The second type is characterized by structureless or convolute zoning under CL imaging and low to high Th/U ratios (0.01–

Fig. 10. P–T pseudosection calculated using the bulk composition from sample CC31 (assemblage 1). (a) P–T fields of peak assemblage Pl-Kfs-Grt-Bt-Ilm-Qz-Rt-Liq (bold line). (b) Plot of melt vol.%. (c) Plot of Grt Mg# and Grt vol.%. (d) Plot of X_{Grs} and X_{Alm}. (e) Plot of Bt Mg# and Bt vol.%. (f) P–T conditions of equilibration estimated based on overlapping ranges of phase composition and abundance.
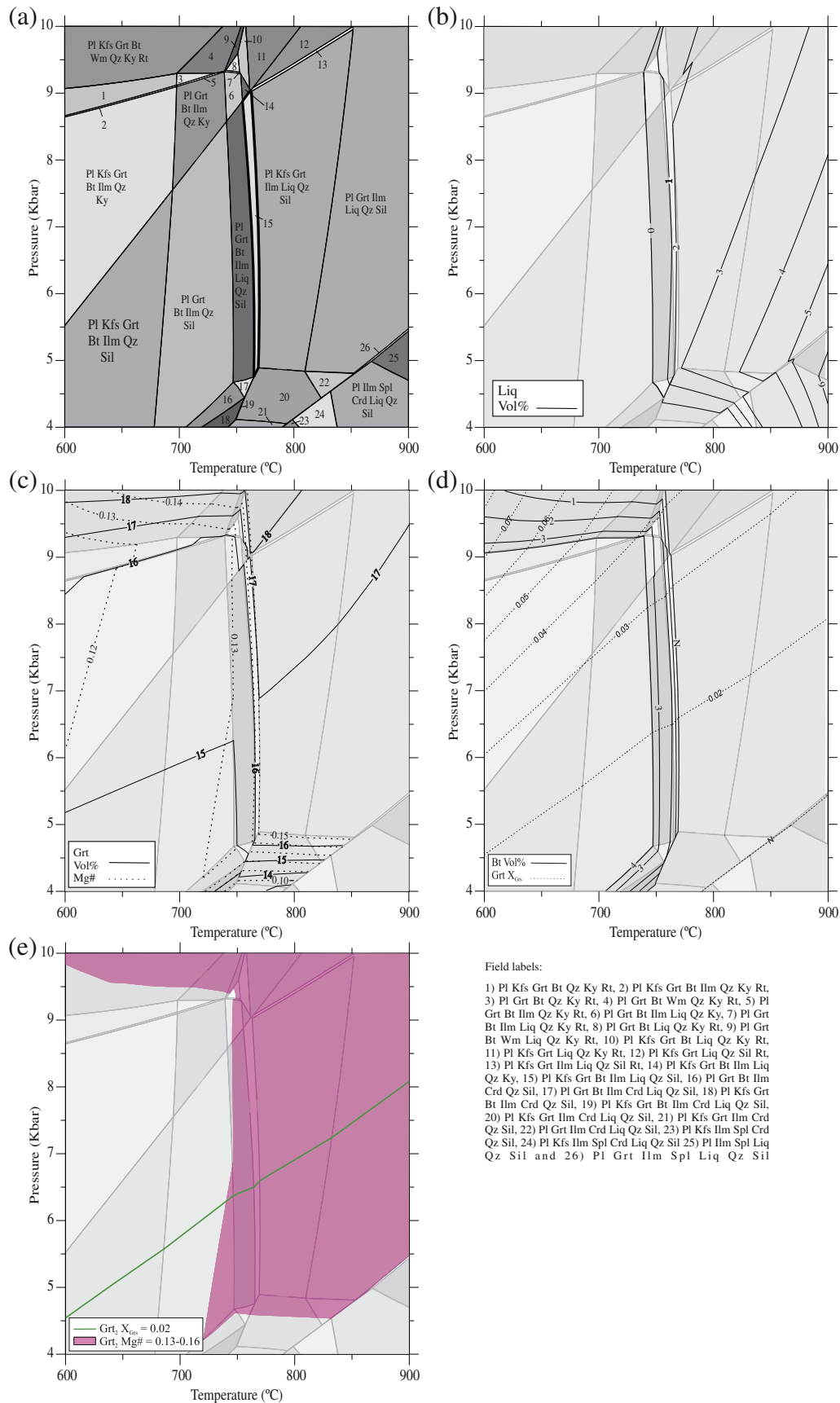
Fig. 11. *P–T* pseudosection calculated with bulk composition from sample CC37 (assemblage 2). (a) P–T fields of peak assemblage Pl-Kfs-Grt-Bt-Ilm-Qz-Sil-Liq (bold line). (b) Plots of melt vol.%. (c) Plots of Grt Mg# and Grt vol.%. (d) Plots of X_{Grs} and Bt vol.%. (e) *P–T* conditions of equilibration further constrained by information on garnet composition.
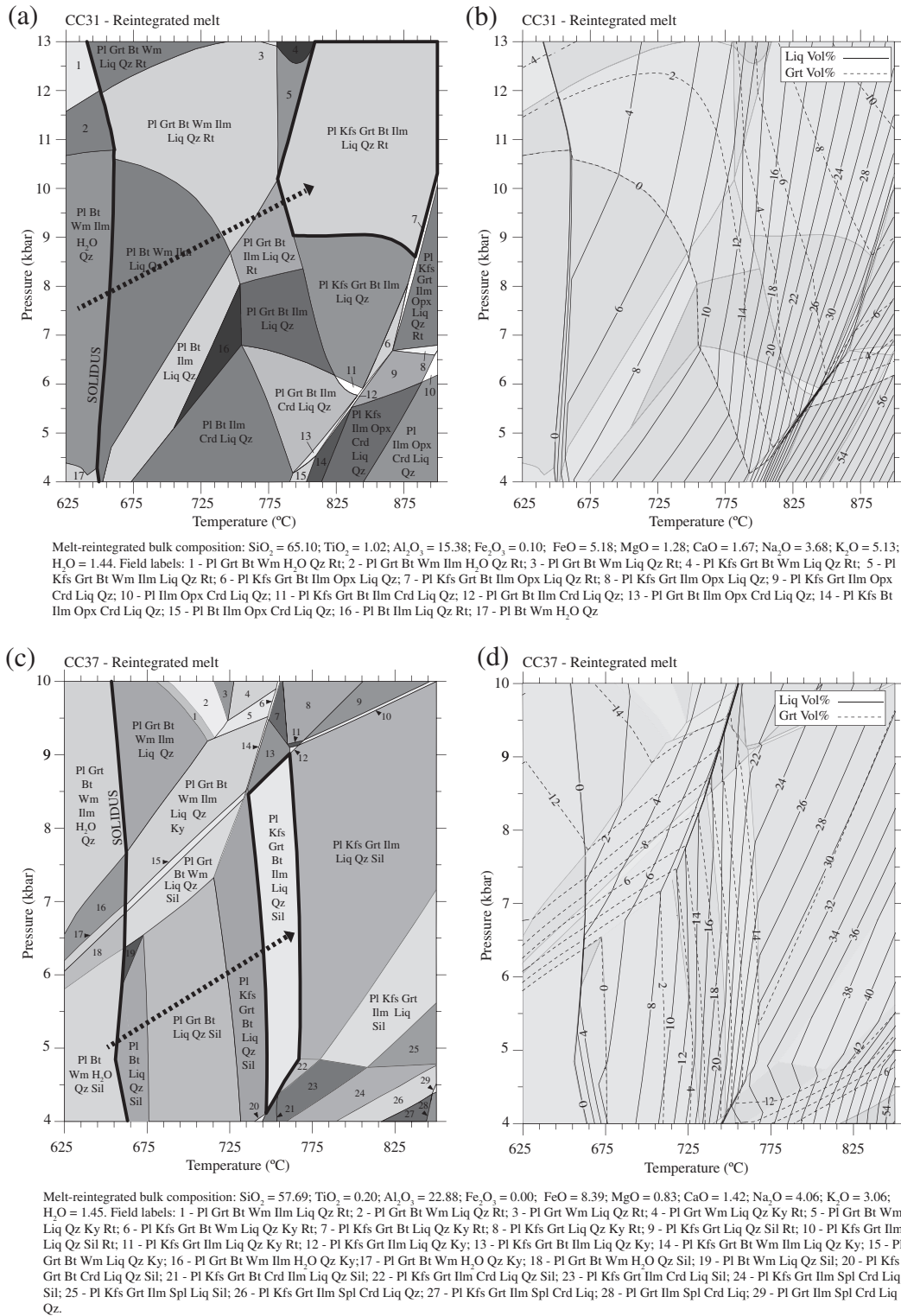
Fig. 12. Melt-reintegrated *P–T* pseudosection for samples CC31 (a,b) and CC37 (c,d) following the method of White et al. (2004). (a) The arrow shows the prograde path from the subsolidus assemblage (Pl-Bt-Wm-Ilm-H_2O-Qz) towards peak metamorphism indicated by bold line (Pl-Kfs-Grt-Bt-Ilm-Qz-Rt-Liq). (b) Plots of Melt vol.% and Grt vol.%. (c) The arrow indicates the prograde path from the subsolidus assemblage (Pl-Bt-Wm-H_2O-Qz-Sil) towards peak metamorphism assemblage (Pl-Kfs-Grt-Bt-Ilm-Qz-Sil-Liq) indicated by bold line. (d) Plots of Melt vol.% and Grt vol.%.

2.51). Ten spot analyses yield a mean $^{206}Pb/^{238}U$ age of 562 ± 4 Ma (95% conf., MSWD = 0.64). The last variety presents brighter cores and fine darker rims in CL imaging, moderate to high Th/U ratios (1.06–1.53) and it occurs together with ilmenite, adjacent to the poikiloblastic garnet crystals. Five spot analyses in brighter domains produced a mean $^{206}Pb/^{238}U$ age of 528 ± 5 Ma (95% conf., MSWD = 0.37).

8.2. Sample CC37 – assemblage 2

This sample yielded 50 to 280 μm, prismatic, subhedral/euhedral to subrounded zircon grains. CL imaging displays strongly luminescent or oscillatory-zoned to irregular zoning cores truncated by darker structureless overgrowths and convoluted zoning (Fig. 14c).

Table 3
Summary of geochronological data showing inherited, crystallization and metamorphism ages for the Carlos Chagas batholith.

Samples	Textural context	Inherited age (Ma)	Crystallization age (Ma)	Metamorphism age (Ma)		
Monazite						
CC31	Grt$_1$(c)	617 ± 12 (n = 25)		560 ± 9 (n = 6)	521 ± 14 (n = 1)	
	ad_Grt$_1$				519 ± 14 (n = 1)	
	M	612 ± 17 (n = 1)		562 ± 11 (n = 2)		492 ± 16 (n = 4)
CC37	Grt$_1$(c)			557 ± 7 (n = 4)		
	Grt$_1$(r)			569 ± 14 (n = 1)	528 ± 14 (n = 1)	
	M			558 ± 10 (n = 8)		484 ± 13 (n = 1)
CC21	Grt$_1$(c)			566 ± 16 (n = 1)	535 ± 14 (n = 1)	
	Grt$_1$(c)			552 ± 15 (n = 1)	516 ± 14 (n = 1)	
	Grt$_2$(c)				515 ± 14 (n = 1)	
	M			562 ± 5 (n = 8)	527 ± 14 (n = 1)	485 ± 9 (n = 2)
Zircon						
CC31	Grt$_1$(c)			563 ± 9 (n = 2)		
	Grt$_1$(r)			543 ± 9 (n = 2)		
	M		577 ± 6 Ma (n = 4)	562 ± 4 (n = 10)	528 ± 5 Ma (n = 5)	
CC37		706 ± 15 (n = 1)	576 ± 3 Ma (n = 14)	562 ± 5 (n = 6)	530 ± 4 Ma (n = 8)	
		607 ± 4 (n = 10)				
CC21	Grt$_1$(c)			564 ± 4 (n = 7)		

Textural context of the monazite and zircon: Grt$_1$(c), monazite/zircon grain included in poikiloblastic garnet core; Grt$_1$(r), monazite/zircon grain included in poikiloblastic garnet rim; Grt$_2$(c), monazite grain included in smaller garnet core; ad_Grt$_1$, monazite grain adjacent or touching poikiloblastic garnet rim; M, monazite/zircon grain in the matrix. n = number of analyses.

Ten spot analyses on CL-defined inherited cores (strongly luminescent cores) have variable Th/U values of 0.03–0.49 and yield a mean ^{206}Pb/^{238}U age of 607 ± 4 Ma (95% conf., MSWD = 0.90). One spot

has an older inherited ^{206}Pb/^{238}U age of 706 ± 15 Ma and a Th/U ratio of 0.10. Based on the Th/U ratio obtained in fourteen analyses from the brighter zircon cores with oscillatory to irregular zoning, two
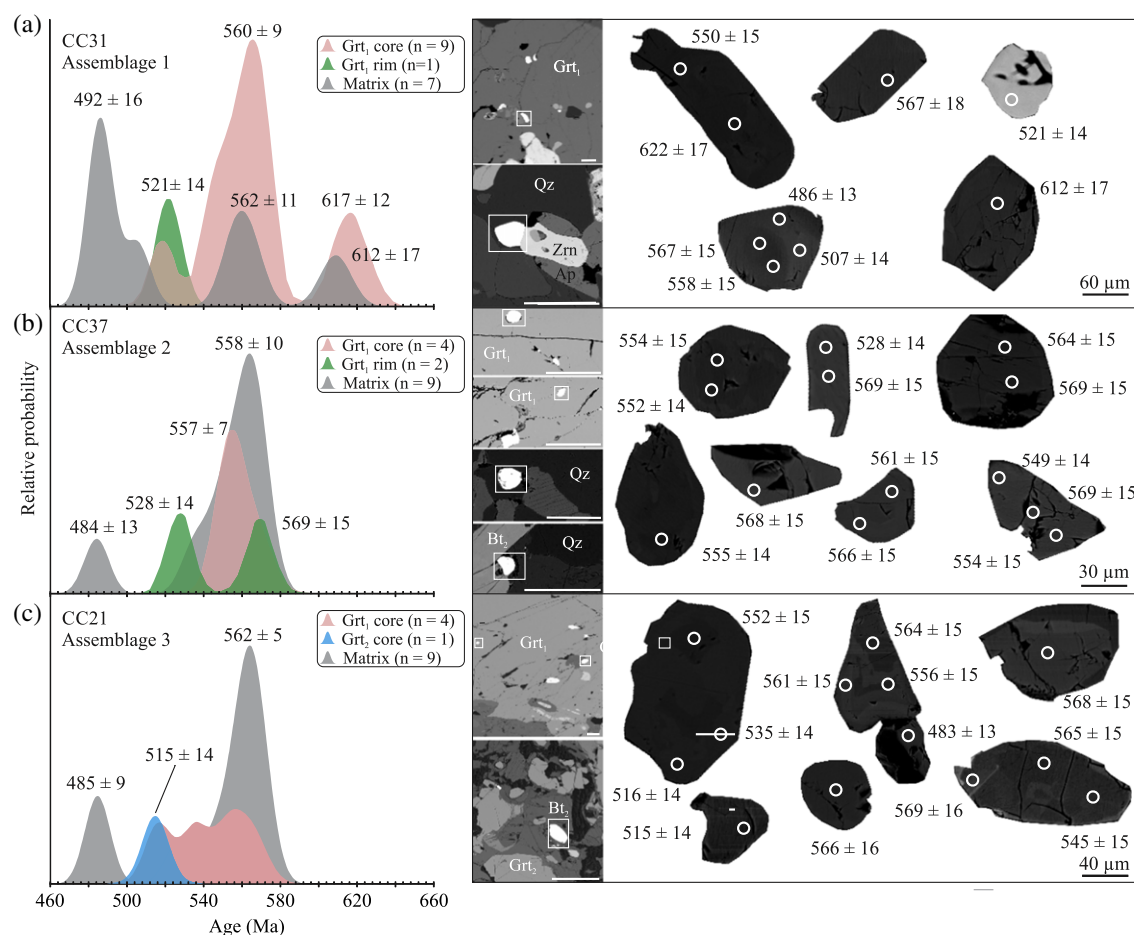

Fig. 13. Histogram of monazite age data using the mean ^{206}Pb/^{238}U age and representative BSE images for monazite grains analyzed in this study. The microstructure position of monazite analyzed in each sample is indicated by white rectangles. (a) Histogram of inherited and metamorphic monazite grains obtained from sample CC31 (assemblage 1). BSE images display unzoned internal structure to weakly zoned grains. (b) Histogram of metamorphic monazite included in Grt$_1$ and matrix from sample CC37 (assemblage 2). Some grains show darker core surrounded by fine brighter rim in BSE images (c) Histogram showing metamorphic monazite age obtained in the matrix and Grt$_1$ and Grt$_2$ crystals from sample CC21 (assemblage 3). Matrix monazite displays patchy zoning via BSE images. Scale bar is equal to 200 μm for the textural position of analyzed grains.
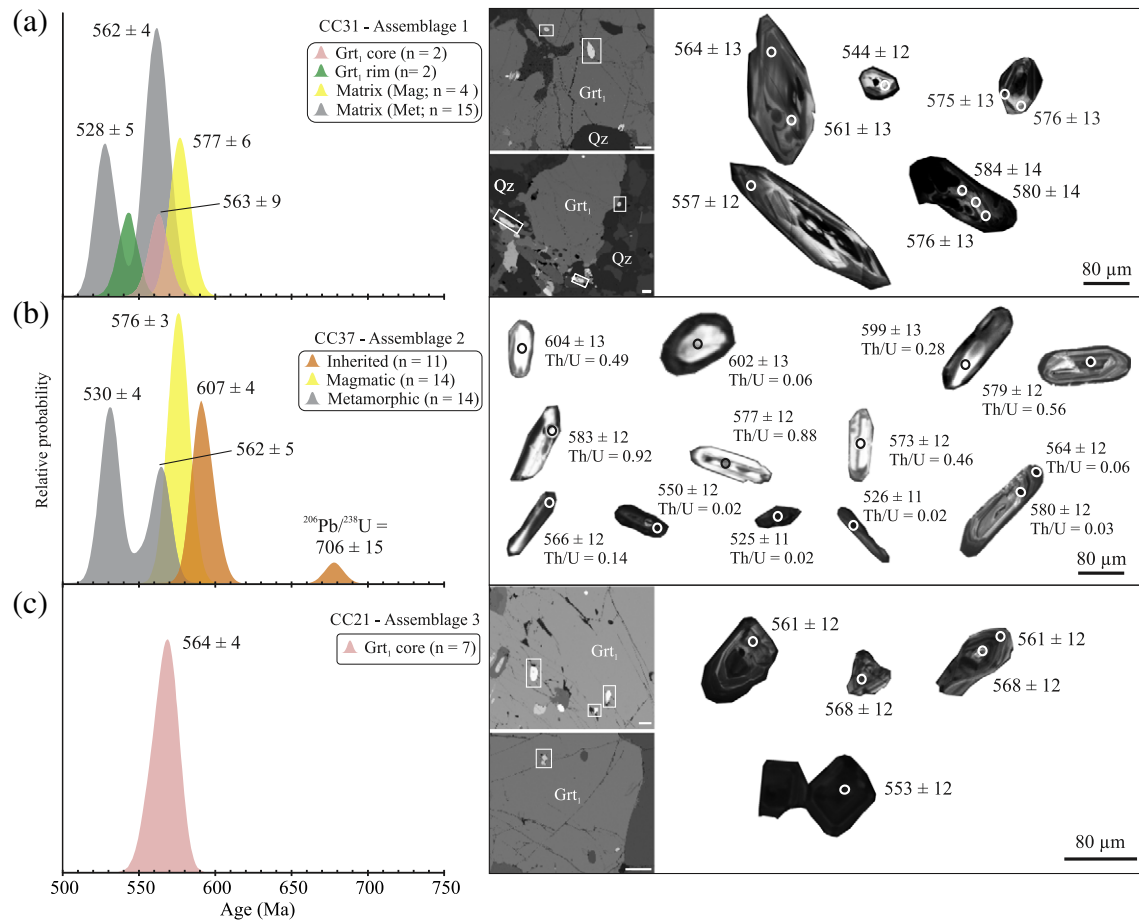
Fig. 14. Histogram and representative cathodoluminescence images of zircons from CCB. The microstructure position of zircon analyzed in each sample is indicated by white rectangles. (a) Histogram displaying $^{206}Pb/^{238}U$ age of zircon included in Grt_1 and matrix from sample CC31 (assemblage 1). Zircon show convoluted zonation typical of high-grade metamorphism. (b) Histogram showing main $^{206}Pb/^{238}U$ age of inherited, magmatic and metamorphic zircons from sample CC37 (assemblage 2). Zircon comprising strongly luminescent inherited core and irregular zoning magmatic core truncated by darker rim. (c) Histogram showing main $^{206}Pb/^{238}U$ age of zircon included in Grt_1 from sample CC21 (assemblage 3). Zircon displays irregular zoning. Scale bar is equal to 200 µm for the textural position of analyzed grains.

different populations were distinguished: low (0.02–0.06) and high Th/U (0.28–0.92) ratios. However, both populations are age equivalent within analytical uncertainties and provide a mean $^{206}Pb/^{238}U$ age of 576 ± 3 Ma (95% conf., MSWD = 0.35). Six out of fourteen spot analyses performed on the darker and structureless zircon grains, with Th/U values between 0.02 and 0.14, yielded a mean $^{206}Pb/^{238}U$ age of 562 ± 5 Ma (95% conf., MSWD = 1.15). Eight additional analyses on the structureless zircon grains also have low Th/U ratio (0.02–0.16) and show a mean $^{206}Pb/^{238}U$ age of 530 ± 4 Ma (95% conf., MSWD = 0.38).

8.3. Sample CC21 – assemblage 3

Zircon grains are prismatic, subhedral to euhedral, ranging from 25 to 150 µm. CL images reveal recrystallization features typical of granulite facies zircon, such as convoluted zoning and darker cores truncated by irregular zoning (Fig. 14b). Seven spot analyses from zircon within Grt_1 core, with Th/U values between 0.03 and 0.39, yield a mean $^{206}Pb/^{238}U$ age of 564 ± 4 Ma (95% conf., MSWD = 1.01).

9. Discussion and conclusions

This work has uncovered two previously unrecognized anatectic events that have affected the entire Carlos Chagas batholith. This polymetamorphic anatectic history has not been identified by previous regional geological investigations due to the fact that the ubiquitous megacrystic K-feldspar crystals that characterize the CCB were not

involved in the melting processes which, in both events, primarily consumed biotite, quartz and plagioclase in the matrix interstitial to the megacrysts. The reason for this is that biotite fluid-absent melting reactions are close to degeneracy with regard to K-feldspar and either produce or consume only small amounts of K-feldspar, depending on the specifics of pressure of melting and bulk composition (e.g. Carrington and Watt, 1995). In the CCB this results in anatectic events that are not obvious without detailed textural and quantitative mineral chemical analysis. The evidence for anatexis of the CCB, the timing of anatexis and the P–T paths relevant to the anatectic events are discussed below.

9.1. U–Pb ages of monazite and zircon from the Carlos Chagas batholith

The ages of 577 ± 6 Ma (CC31) and 576 ± 3 Ma (CC37) obtained from oscillatory-zoned or irregular zoned cores of zircon, with variable Th/U ratios (0.02–1.29), are interpreted as best representing the crystallization age of the batholith (Fig. 14a,b; Table 3). This is in agreement with previous studies which have demonstrated that the syn-collisional granites in the Araçuaí orogen were emplaced between 585 and 545 Ma, with the dominant magmatic age being ca. 575 Ma (Gradim et al., 2014; Pedrosa-Soares et al., 2011; Richter et al., 2016; Roncato, 2009; Silva et al., 2002, 2005; Vauchez et al., 2007).

U–Pb ages of some monazite cores found within Grt_1 and in the matrix (CC31) give ages of 617 ± 12 Ma and 612 ± 17 Ma (Fig. 13a; Table 3), respectively. These grains can be interpreted as inherited

monazite from the source of the CCB. This interpretation is consistent with other studies in granulitic rocks worldwide (e.g. Hermann and Rubatto, 2003; Montel et al., 2000) and experimental studies (e.g. Cherniak et al., 2000), which demonstrate that monazite can persist during high-grade metamorphism and anatexis. As illustrated by CL-images in Fig. 14b, some zircon grains show strongly luminescent cores with low to moderate Th/U ratios (0.03–0.49) rimmed by darker and structureless domains. These zircon cores are interpreted as inherited and present a dominant age peak at 607 ± 4 Ma (Fig. 14b), which is similar, within analytical error, to the inherited monazite age (Fig. 13a). The NVC records a peak in the age distribution of detrital zircon and monazite grains at ca. 606–612 Ma (Richter et al., 2016), which is similar to the age of inherited grains from the CCB, possibly indicating the Rio Doce (Pedrosa-Soares et al., 2011) and/or Rio Negro (Heilbron and Machado, 2003) magmatic arcs as representing material similar to the source of the CCB. A single zircon grain with the oldest recorded age in this study (706 ± 15 Ma; Fig. 14b) may correlate with reported ages from the Southern Bahia Alkaline Province (ca. 696–732 Ma; Rosa et al., 2007), which is related to the rift episode along the southern part of the São Francisco craton.

Geochronology on monazite and zircon inclusions in Grt_1 yielding ages from 569 ± 14 to 552 ± 15 Ma (Table 3) and are interpreted as age of peak of the first metamorphic event (M1) in the CCB. This age interval is equal, within analytical error, to the oldest monazite (from 562 ± 11 to 558 ± 10 Ma; Table 3) and zircon (562 ± 4 Ma; Table 3) ages found in the matrix, implying that these grains were formed at peak metamorphism. Zircon crystals handpicked from the whole rock aliquot of CC37 also revealed a similar age of 562 ± 5 Ma (Fig. 14b; Table 3) and are interpreted to be metamorphic because of their lack of zonation (Fig. 14b) and low Th/U ratios (0.02–0.14). Metamorphic ages such as these have also found in NVC (ca. 575–560 Ma; Gradim et al., 2014; Richter et al., 2016).

The second metamorphic event (M2) affected all the CCB rocks (assemblages 1, 2 and 3) at ca. 535–515 Ma, as indicated by monazite and zircon ages in this study (Figs. 13 and 14). Monazite inclusions within Grt_2 which clearly texturally post-dates Grt_1, give an age of 515 ± 14 Ma (CC21), defining the age of M2. In addition, zircon rims that are relatively dark in CL images (Fig. 14a,b) yielded ages of 528 ± 5 Ma (n = 5; CC31 – Fig. 14a) and 530 ± 4 Ma (n = 8; CC37 - Fig. 14b), which are within analytical uncertainties of those monazite ages included in Grt_2. We interpreted the monazite ages ranging from 535 ± 14 Ma to 516 ± 14 Ma (Table 3) obtained from the rims of Grt_1 to be metamorphic ages produced due to interaction with fluid/melt along microcracks in the garnet during the second metamorphic event (M2).

The M2 age is not widely documented in the Araçuaí orogen and some studies have interpreted the youngest metamorphic ages as Pb-loss disturbance due to post-collisional intrusions (Silva et al., 2002). Richter et al. (2016) have also reported metamorphic ages of ca. 523–495 Ma for monazite and zircon from the NVC and G2 granites.

The youngest ages recorded in this study of 492 ± 16 Ma (n = 4; CC31), ca. 484 ± 13 Ma (n = 1; CC37) and ca. 485 ± 9 Ma (n = 2; CC21) were found in matrix monazite (Fig. 13) and can be attributed to later fluid–rock interaction contemporaneous with gravitational collapse of the Araçuaí orogen (Gradim et al., 2014; Pedrosa-Soares et al., 2011). Fluid movement through the crust at this time is supported by hydrothermal gem deposits (e.g., emerald, alexandrite and/or aquamarine) from districts of the Eastern Pegmatite Province in the Araçuaí orogen (Pedrosa-Soares et al., 2011).

9.2. First period of garnet growth (Grt_1)

The PT conditions of formation indicated by the peak assemblage 1 (Pl-Kfs-Grt-Bt-Ilm-Qz-Rt-Liq; Figs. 10 and 11) are consistent with the occurrence of incongruent melting reactions consuming biotite, as constrained by experiments and studies of peraluminous metasedimentary migmatitic granulites (Johnson et al., 2008; Nicoli

et al., 2015; Patiño Douce and Beard, 1996; Richter et al., 2016; Stevens et al., 1997; Vielzeuf and Montel, 1994). Therefore, the poikiloblastic garnet crystals (Grt_1) in all parts of the CCB (assemblages 1, 2 and 3) are interpreted as a product of partial melting reactions that consumed high-Ti biotite, quartz and plagioclase at granulite facies conditions and produced peritectic phases (garnet and rutile) and melt. Microstructures such as, films and pools of plagioclase and/or quartz occur both in the matrix and surrounding Grt_1 crystals (Figs. 4d,e and 5e,f,g,h). These microstructures are typically interpreted to represent melt pseudomorphs. Further to that, abundant rounded inclusions of Ti-biotite in Grt_1 indicate that garnet grew at the expense of Bt and corroborate the interpretation that melting was ongoing (Fig. 4b,c).

Grt_1 is unzoned in terms of major elements (Supplementary data - Table 1; Figs. 6 and 7a), yet displays a slight zoning of HREE (Supplementary data - Table 2, Fig. 8). Its negative Eu anomaly (Fig. 8) indicates that garnet was in equilibrium with K-feldspar, as expected from the phase equilibrium modeling.

In addition to the grossular content of Grt_1 (assemblage 1), the peak pressure of this event can be constrained by the presence of ilmenite and rutile. Taken into consideration the phase equilibrium modeling for samples CC28 and CC31 (Figs. 9a and 10a), the field of the peak assemblage 1 is stable between 780 and 870 °C and 8.9–13.4 kbar. Based on the $X_{Grs} + X_{Alm} + Grt_{Mg\#} + Bt_{Mg\#}$ isopleths, we infer that M1 event reached 790–820 °C and 9.5–10.5 kbar (Figs. 9f and 10f). Assuming the average density of the crust to be 2.75 g/cm^3 these conditions translate to depths of 26–29 km with a geothermal gradient up to 28–30 °C km^{-1} (Fig. 15).

The CCB records higher pressure conditions than the adjacent paragneisses complexes which record peak pressures below 8 kbar (e.g. Gradim, 2013; Munhá et al., 2005; Richter et al., 2016). According to Richter et al. (2016) rocks of the nearby NVC sediments were buried to at least 25 km at ca. 570 Ma suggesting that the currently exposed units in the core of the AO were buried to varied depths and were differentially exhumed during cooling, with the CCB representing rocks that at the time of peak metamorphism were below the paragneiss complexes that now surround the batholith. In the Araçuaí orogen, east–west verging shear zones developed along the major lithological contacts appear to have accommodated the differential motion of blocks (Alkmim
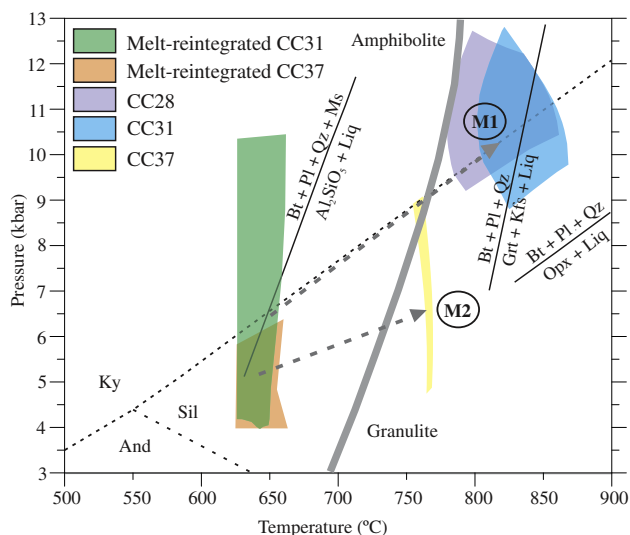

Fig. 15. Suggested *P–T* conditions for Carlos Chagas batholith. Peak metamorphism in studied samples was attained at granulite conditions and both generations of garnet were produced by biotite absent-fluid melting reactions. Reaction curves after partial melting experiments (Patiño Douce and Johnston, 1991; Stevens et al., 1997; Vielzeuf and Montel, 1994).

et al., 2006; Castañeda et al., 2006; Pinto et al., 2001; Queiroga et al., 2012).

M1 is interpreted to be a consequence of the collisional stage of orogeny, where crustal thickening probably involved thrusting of the magmatic arc onto the back-arc region (Gradim et al., 2014; Pedrosa-Soares et al., 2011). This event produced most of the garnet in the CCB and the almost complete lack of retrogression of these crystals to biotite indicates that melt loss after this first melting event efficiently removed H_2O from the rock. Pseudosection modeling of the melt-reintegrated bulk composition (Fig. 12a,b) indicates that 12–34 vol.% of melt had been produced by the time peak conditions were attained. Less than 3 vol.% of melt (Figs. 9b and 10b) is inferred to have remained in the rock. This minor remnant melt volume produced the microstructures which corroborate the presence of melt, showing films of melt along garnet boundaries and between plagioclase grains in matrix (Fig. 4d,e). It is also aligned with recent models of melt extractions in which excess melt is drained away and does not leave significant imprint (Yakymchuk and Brown, 2014).

9.3. Second period of garnet growth (Grt_2)

As discussed above, a substantial amount of melt must be removed from the residuum before cooling in order to preserve the peak assemblage. After the M1 event, the CCB was relatively anhydrous with the remnant M1 biotite being the only source of water in the assemblage. Thus, the rocks were unfertile for the further production of melt. This situation was changed along shear zones where fluids were able to infiltrate, most likely under amphibolite to greenschist facies conditions and rehydrate the sheared rocks. This most likely occurred through hydration of K-feldspar and possibly also some minor fraction of Grt_1 along the shear fabric to produce an anastomosing muscovite-biotite fabric. These hydrated domains were the only portions of the CCB that were susceptible to further anatexis during the M2 event, which resulted in muscovite breakdown to produce sillimanite on the second metamorphic event (M2) prograde path. The presence of sillimanite and the locally higher water activity allowed a second melting reaction to occur which consumed biotite, sillimanite, plagioclase and quartz, and which produced peritectic Grt_2 (Figs. 3g and 5a,b).

Indeed, the microstructures show that Grt_1 crystals produced during M1 melting are free of sillimanite inclusions (e.g., Fig. 4b,c) and therefore it is very unlikely that the CCB contained sillimanite during M1. Thus, sillimanite was a product of deformation and metamorphism associated with M2, in the previously rehydrated rocks (assemblages 2 and 3). Sillimanite occurs in such rocks as prismatic aggregates in the matrix and also as needles inclusions in the 2nd generation of garnet (Fig. 5a,b). These petrographic observations indicate that this Grt_2 is likely to have formed as a consequence fluid-absent melting reaction at the expense of biotite and sillimanite during M2 event. In addition, pseudomorphed thin melt films are documented surrounding of Grt_2 crystals (Fig. 5h), implying that garnet grew in the presence of melt.

Phase equilibrium modeling using the bulk compositions of small domains (e.g. CC37 – assemblage 2) indicate that the inferred peak metamorphic mineral assemblage (Pl-Kfs-Grt-Bt-Ilm-Qz-Sil-Liq) equilibrated at 770 °C and 6.6 kbar (Fig. 11e). These conditions correspond to depths of ~18 km with a geothermal gradient up to 42 °C km^{-1} (Fig. 15). The M2 peak metamorphic estimates are in agreement with garnet formation via an incongruent melting reaction that consumed biotite and sillimanite. This is confirmed by comparison with previous experimental studies (Patiño Douce and Harris, 1998; Patiño Douce and Johnston, 1991; Pickering and Johnston, 1998) and studies of peraluminous metasedimentary migmatites (Richter et al., 2016). Furthermore, the absence of composition zonation and enrich in HREE (Figs. 7 and 9) support that garnet has grown at granulite-facies conditions. Pedrosa-Soares et al. (2011) published temperatures of 642–683 °C (average T method by THERMOCALC) for the Qz + Kfs + Pl + Grt + Bt + Sil assemblage from the CCB. However, these temperatures

conditions are inconsistent with mineral compositions documented in this study and with the microtextures indicating the coexistence of melt and Grt_2. The pseudosection modeling melt-reintegrated indicates 16–30 vol.% of melt was produced at peak conditions (Fig. 12d).

M2 heating is probably related to asthenosphere ascendance during the extensional thinning and gravitational collapse of the orogen (De Campos et al., 2016; Gradim et al., 2014; Moraes et al., 2015; Pedrosa-Soares et al., 2011), which provided sufficient heat to induce a second anatectic event in the CCB. The G5 supersuite (ca. 525–480 Ma) was emplaced during this extensional episode along pre-existing structures at depths of ~20 km (Baltazar et al., 2010; De Campos et al., 2004, 2016; Gradim et al., 2014; Mendes and De Campos, 2012; Mendes et al., 2005; Noce et al., 2000; Silva et al., 2005).

9.4. Regional implications

The evolution and development of the Araçuaí orogen is marked by a long history of granite production between 630 and 480 Ma (G1 to G5 Supersuites - Pedrosa-Soares et al., 2011). The evidence described in this work indicates three episodes of crustal recycling in the Araçuaí orogeny. In the first event, source rocks with a volume substantially larger than that of the CCB melted to produce a hydrous, peraluminous granitic melt that intruded at presumably higher crustal level within the orogenic belt at ca. 575 Ma. At least part of the water in this hydrous magma was trapped due to biotite crystallization producing a fertile granite. Thickening and further evolution of the orogen buried the CCB producing a second process of crustal melting, some 15 Ma after the first. Melting and melt extraction produced an almost completely anhydrous and refractory rock. The third and final episode occurred only where hydration due to shearing had refertilized the CCB for melt generation and produced relatively minor melt volumes, which were lost leaving the CCB dry and refractory. Recognizing repeated partial melting events involving granites during an orogeny provides the key for understand the mid- to lower crustal tectonic recycling in an exhumed orogenic belt and interpreting complex zircon and monazite age distributions.

Acknowledgements

Appendix A. Supplementary data

Supplementary data to this article can be found online at http://dx.doi.org/10.1016/j.lithos.2016.10.012.

References

Alkmim, F.F., Marshak, S., Pedrosa-Soares, A.C., Peres, G.G., Cruz, S.C.P., Whittingyon, A., 2006. Kinematic evolution of the Araçuaí-West Congo orogen in Brazil and Africa: nutcracker tectonics during the Neoproterozoic assembly of Gondwana. Precambrian Research 149, 43–64.

Baltazar, O.F., Zuchetti, M., Oliveira, S.A.M., Scandolara, J., Silva, L.C., 2010. Folhas São Gabriel Da Palha e Linhares. Nota Explicativa. Programa Geologia do Brasil, CPRM-BH (144 pp.).

Belém, J., 2014. Geoquímica, Geocronologia e Contexto geotectônico Do Magmatismo máfico Associado Ao Feixe de Fraturas Colatina, Estado Do Espírito Santo. Instituto de Geociências, Universidade Federal de Minas Gerais, Belo Horizonte (Phd Thesis, 134 pp.).

Brown, M., 1994. The generation, segregation, ascent and emplacement of granite magma: the migmatite-to-crustally-derived granite connection in thickened orogens. Earth-Science Reviews 36, 83–130.

Brown, M., 2010. Melting of the continental crust during orogenesis: the thermal, rheological, and compositional consequences of melt transport from lower to upper continental crust. Canadian Journal of Earth Sciences 47, 655–694.

Brown, M., 2013. Granite: from genesis to emplacement. Geological Society of America Bulletin 125, 1079–1113.

Brown, M., Rushmer, T., 2006. Evolution and Differentiation of the Continental Crust. Cambridge University Press, Cambridge, UK (562 pp.).

Carrington, D.P., Watt, G.R., 1995. A geochemical and experimental study of the role of K-feldspar during water-undersaturated melting of metapelites. Chemical Geology 122, 59–76.

Castañeda, C., Pedrosa-Soares, A.C., Belém, J., Dias, P.H.A., Gradim, D.T., Medeiros, S.R., Oliveira, F.F., 2006. Folha Ecoporanga, SE.24-Y-A-III, escala 1:100.000: nota explicativa Espírito Santo, UFMG/CPRM 80 pp.

Castro, A., Patiño Douce, A.E., Corretgé, L.G., De la Rosa, J.D., El-Biad, M., El-Hmidi, H., 1999. Origin of peraluminous granites and granodiorites, Iberian massif, Spain: and experimental test of granite petrogenesis. Contributions to Mineralogy and Petrology 135, 255–276.

Cavalcante, G.C.G., Egydio-Silva, M., Vauchez, A., Camps, P., Oliveira, E., 2013. Strain distribution across a partially molten middle crust: insights from the AMS mapping of the Carlos Chagas Anatexite, Araçuaí belt (East Brazil). Journal of Structural Geology 55, 79–100.

Chappell, B.W., White, A.J.R., 1974. Two contrasting granite types. Pacific Geology 8, 173–174.

Cherniak, D.J., Watson, B.E., Harrison, M.T., Grove, M., 2000. Pb diffusion in monazite: a progress report on a combined RBS/SIMS study. Eos Transactions 41 (19), S25.

Coggon, R., Holland, T.J.B., 2002. Mixing properties of phengitic micas and revised garnet–phengite thermobarometers. Journal of Metamorphic Geology 20, 683–696.

Collins, W.J., Richards, S.W., 2008. Geodynamic significance of S-type granites in circum-Pacific orogens. Geology 36, 559–562.

De Campos, C.P., Mendes, J.C., Ludka, I.P., Medeiros, S.R., Moura, J.C., Wallfass, C., 2004. A review of the Brasiliano magmatism in southern Espírito Santo, Brazil, with emphasis on post-collisional magmatism. Journal of the Virtual Explorer 17.

De Campos, C.P., Medeiros, S.R., Mendes, J.C., Pedrosa-Soares, A.C., Dussin, I, Ludka, I.P., Dantas, E.L., 2016. Cambro-Ordovician magmatism in the Araçuaí Belt (SE Brazil): snapshots from a post-collisional event. Journal of South American Earth Sciences 68, 248–268.

De Capitani, C., Petrakakis, K., 2010. The computation of equilibrium assemblage diagrams with Theriak/Domino software. American Mineralogist 95, 1006–1016.

Droop, G.T.R., 1987. A general equation for estimating Fe^{3+} concentrations in ferromagnesian silicates and oxides from microprobe analyses, using stoichiometric criteria. Mineralogical Magazine 51, 431–435.

Gradim, C.T., 2013. Complexo Nova Venécia e Magmatismo Associado, Orógeno Araçuaí, Estado Do Espírito Santo. Instituto de Geociências, Universidade Federal de Minas Gerais, Belo Horizonte (MSc Dissertation, 96 pp.).

Gradim, C.T., Queiroga, G.N., Roncato, J.G., Novo, T.A., Pedrosa-Soares, A.C., 2007. Mapa Geológico da Folha Mantena 1: 100.000 Belo Horizonte, Programa Geologia do Brasil, CPRM-UFMG.

Gradim, C., Roncato, J., Pedrosa-Soares, A.C., Cordani, U., Dussin, I., Alkmim, F.F., Queiroga, G., Jacobssohn, T., Silva, L.C., Babinski, M., 2014. The hot back-arc zone of the Araçuaí orogen, Eastern Brazil: from sedimentation to granite generation. Brazilian Journal of Geology 44, 155–180.

Heilbron, M., Machado, N., 2003. Timing of terrane accretion in the Neoproterozoic-Eopaleozoic Ribeira Orogen (SE Brazil). Precambrian Research 125, 87–112.

Hermann, J., Rubatto, D., 2003. Relating zircon and monazite domains to garnet growth zones: age and duration of granulite facies metamorphism in the Val Malenco lower crust. Journal of Metamorphic Geology 21, 833–852.

Holland, T.J.B., Powell, R., 1998. An internally consistent thermodynamic data set for phases of petrological interest. Journal of Metamorphic Geology 16, 309–343.

Holland, T., Powell, R., 2003. Activity–composition relations for phases in petrological calculations: an asymmetric multicomponent formulation. Contributions to Mineralogy and Petrology 145, 492–501.

Jeon, H., Williams, I.S., Chappell, B.W., 2012. Magma to mud to magma: rapid crustal recycling by Permian granite magmatism near the eastern Gondwana margin. Earth and Planetary Science Letters 319-320, 104–117.

Johnson, T.E., White, R.W., Powell, R., 2008. Partial melting of metagreywacke - a calculated mineral equilibria study. Journal of Metamorphic Geology 26, 837–853.

McDonough, W.F., Sun, S.S., 1995. The composition of the Earth. Chemical Geology 120, 223–253.

Mendes, J.C., De Campos, C.M.P., 2012. Norite and charnockites from the Venda Nova Pluton, SE Brazil: intensive parameters and some petrogenetic constraints. Geoscience Frontiers 3, 789–800.

Mendes, J.C., Medeiros, S.R., McReath, I., De Campos, C.M.P., 2005. Cambro-Ordovician magmatism in SE Brazil: U–Pb ages, combined with Sr and Nd isotopic data of charnockitic rocks from the Varzea Alegre complex. Gondwana Research 8, 337–345.

Montel, J.M., Kornprobst, J., Vielzeuf, D., 2000. Preservation of U-Th-Pb ages in shielded monazite: example from the Beni Bousera Hercynian Kinzigites (Morocco). Journal of Metamorphic Geology 18, 335–342.

Moraes, R., Nicollet, C., Barbosa, J.S.F., Fuck, R.A., Sampaio, A.R., 2015. Applications and limitations of thermobarometry in migmatites and granulites using as an example rocks of the Araçuaí Orogen in southern Bahia, including a discussion on the tectonic meaning of the current results. Brazilian Journal of Geology 45, 517–539.

Munhá, J.M.U., Cordani, U.G., Tassinari, C.C.G., Palácios, T., 2005. Petrologia e termocronologia de gnaisses migmatíticos da faixa de dobramentos Araçuaí (Espírito Santo, Brasil). Revista Brasileira de Geociências 35, 123–134.

Nicoli, G., Stevens, G., Moyen, J.F., Frei, D., 2015. Rapid evolution from sediment to anatectic granulite in an Archean continental collision zone: the example of the Bandelierkop Formation metapelites, South Marginal Zone, Limpopo Belt, South Africa. Journal of Metamorphic Geology 33, 177–202.

Noce, C.M., Macambira, M.J.B., Pedrosa-Soares, A.C., 2000. Chronology of Neoproterozoic-Cambrian granitic magmatism in the Araçuaí Belt, eastern Brazil, based on single zircon evaporation dating. Revista Brasileira de Geociencias 30, 25–29.

Noce, C.M., Pedrosa-Soares, A.C., Piuzana, D., Armstrong, R., Laux, J.H., De Campos, C.M., Medeiros, S.R., 2004. Ages of sedimentation of the kinzigitic complex and of a late orogenic thermal episode in the Araçuaí orogen, northern Espírito Santo state, Brazil: zircon and monazite U–Pb SHRIMP and IDTIMS data. Revista Brasileira de Geociencias 34, 587–592.

Patiño Douce, A.E., Beard, J.S., 1996. Effects of P, $f(O_2)$ and Mg/Fe ratio on dehydration melting of model metagreywackes. Journal of Petrology 37, 999–1024.

Patiño Douce, A.E., Harris, N., 1998. Experimental constraints on Himalayan anatexis. Journal of Petrology 39, 689–710.

Patiño Douce, A.E., Johnston, A.D., 1991. Phase equilibria and melt productivity in the pelitic system: implications for the origin of peraluminous granitoids and aluminous granulites. Contributions to Mineralogy and Petrology 107, 202–218.

Pedrosa-Soares, A.C., Noce, C.M., Wiedemann, C., Pinto, C.P., 2001. The Araçuaí-West-Congo Orogen in Brazil: an overview of a confined orogen formed during Gondwanaland assembly. Precambrian Research 110, 307–323.

Pedrosa-Soares, A.C., Queiroga, G.N., Gradim, C.T., Roncato, J.G., Novo, T.A., Jacobsohn, T., Silva, K.L., 2006. Geologia Da Folha Mantena (SE-24-Y-A-VI). Programa Geologia do Brasil, CPRM (82pp. http://geobank.cprm.gov.br).

Pedrosa-Soares, A.C., Noce, C.M., Alkmim, F.F., Silva, L.C.S., Babinski, M., Cordani, U., Castañeda, C., 2007. Orógeno Araçuaí: síntese do conhecimento 30 anos após Almeida 1977. Geonomos 15, 1–16.

Pedrosa-Soares, A.C., Alkmim, F.F., Tack, L., Noce, C.M., Babinski, M., Silva, L.C., Martins-Neto, M., 2008. Similarities and differences between the Brazilian and African counterparts of the Neoproterozoic Araçuaí West Congo Orogen. In: Pankhurst, J.R., Trouw, R.A.J., Brito Neves, B.B., De Wit, M.J. (Eds.), West Gondwana: Pre-Cenozoic Correlations across the South Atlantic Region. Geological Society of London, Special Publications vol. 294, pp. 153–172.

Pedrosa-Soares, A.C., De Campos, C.P., Noce, C., Silva, L.C., Novo, T., Roncato, J., Medeiros, S., Castañeda, C., Queiroga, G., Dantas, E., Dussin, I., Alkmim, F., 2011. Late Neoproterozoic–Cambrian granitic magmatism in the Araçuaí orogen (Brazil), the Eastern Brazilian Pegmatite Province and related mineral resources. Geological Society of London, Special Publication 350, 25–51.

Peixoto, E., Pedrosa-Soares, A.C., Alkmim, F.F., Dussin, I.A., 2015. A suture-related accretionary wedge formed in the Neoproterozoic Araçuaí orogen (SE Brazil) during Western Gondwanaland assembly. Gondwana Research 27, 878–896.

Petford, N., Cruden, A.R., McCaffrey, K.J.W., Vigneresse, J.L., 2000. Granite magma formation, transport and emplacement in the Earth's crust. Nature 408, 669–673.

Pickering, J.M., Johnston, A.D., 1998. Fluid-absent melting behavior of a two-mica metapelite: experimental constraints on the origin of Black Hills granite. Journal of Petrology 39, 1787–1804.

Pinto, C.P., Drumond, J.B.V., Féboli, W.L., 2001. Projeto Leste. CPRM/CODEMIG, CD-ROM, Belo Horizonte.

Queiroga, G.N., Pedrosa-Soares, A.C., Roncato, J.G., Dias, P.H.A., Guimarães, H.A., Coutinho, M.O.G., Freitas, N.C., Gradim, C.T., Braga, F.C.S., Novo, T.A., 2012. Geologia e recursos mineras da Folha Nova Venécia SE-24-Y-B-IV Escala 1:100.000, Estado do Espírito Santo Programa Geologia do Brasil, CPRM-UFMG.

Rasband, W.S., 1997–2012. ImageJ. U.S. National Institutes of Health, Bethesda, MD Available at: http://imagej.nih.gov/ij/ (last accessed on May 2014).

Richter, F., Lana, C., Stevens, G., Buick, I., Pedrosa-Soares, A.C., Alkmim, F.F., Cutts, K., 2016. Sedimentation, metamorphism and granite generation in a back-arc region: records from the Ediacaran Nova Venécia Complex (Araçuaí Orogen, Southeastern Brazil). Precambrian Research 272, 78–100.

Roncato, J.G., 2009. As suítes graníticas Tipo-S Do Norte Do Espírito Santo na região Das Folhas Ecoporanga, Mantena, Montanha e Nova Venécia. Instituto de Geociências, Universidade Federal de Minas Gerais, Minas Gerais (MSc Dissertation 102pp.).

Roncato, J.G., Pedrosa-Soares, A.C., Mascarenhas, T.F., Fornero, S.A., Galinari, L.M., Gonçalves, L.T., Queiroga, G.N., Braga, F.C.S., Novo, T.A., 2012. Geologia e recursos mineras da Folha Montanha SE-24-Y-B-I Escala 1:100.000, Estado do Espírito Santo Programa Geologia do Brasil, CPRM-UFMG.

Rosa, M.L.S., Conceição, H., Macambira, M.J.B., Galarza, M.A., Cunha, M.P., Menezes, R.C.L., Marinho, M.M., Filho, B.E.C., Rios, D.C., 2007. Neoproterozoic anorogenic magmatism in the Southern Bahia Alkaline Province of NE Brazil: U–Pb and Pb–Pb ages of the blue sodalite syenites. Lithos 97, 88–97.

Sampaio, A.R., Martins, A.M., Loureiro, H.C., Arcanjo, J.B., Moraes Filho, J.C., Souza, J.D., Pereira, L.H., Couto, P.A., Santos, R.A., Melo, R.C., Bento, R.V., Borges, V.P., 2004. Extremo Sul Da Bahia: Geologia e Recursos Minerais. Arquivos Abertos. CBPM e CPRM.

Silva, L.C., Armstrong, R., Noce, C.M., Carneiro, M.A., Pimentel, M., Pedrosa-Soares, A.C., Leite, C.A., Vieira, V.S., Silva, M.A., Paes, V.J.C., Filho, J.M.C., 2002. Reavaliação da evolução geológica em terrenos Pré-cambrianos brasileiros com base em novos dados U–Pb SHRIMP, parte II: Orógeno Araçuaí, Cinturão Mineiro e Cráton São Francisco meridional. Revista Brasileira de Geociencias 32, 513–528.

Silva, L.C., McNaughton, N.J., Armstrong, R., Hartmann, L.A., Fletcher, I.R., 2005. The neoproterozoic Mantiqueira Province and its African connections: a zircon-based U–Pb geochronologic subdivision for the Brasiliano/Pan-African systems of orogens. Precambrian Research 136, 203–240.

Silva, L.C., Pedrosa-Soares, A.C., Armstrong, R., Noce, C.M., 2011. Determinando a duração do período colisional do Orógeno Araçuaí com base em geocronologia U–Pb de Alta

resolução em zircão: uma contribuição Para a história da amalgamação do Gondwana Ocidental. Geonomos 19, 180–197.

Stevens, G., Clemens, J.D., Droop, G.T.R., 1997. Melt production during granulite-facies anatexis: experimental data from "primitive" metasedimentary protholiths. Contributions to Mineralogy and Petrology 128, 352–370.

Tack, L., Wingate, M.T.D., Liégeois, J.P., Fernandez-Alonso, M., Deblond, A., 2001. Early Neoproterozoic magmatism (1000–910 Ma) of the Zadinian and Mayumbian Groups (Bas-Congo): onset of Rodinian rifting at the western edge of the Congo craton. Precambrian Research 110, 277–306.

Tedeschi, M., Novo, T., Pedrosa-Soares, A.C., Dussin, I., Tassinari, C., Silva, L.C., Gonçalves, L., Alkmim, F., Lana, C., Figueiredo, C., Dantas, E., Medeiros, S., De Campos, C., Corrales, F., Heibron, M., 2016. The Ediacaran Rio Doce magmatic arc revisited (Araçuaí-Ribeira orogenic system, SE Brazil). Journal of South American Earth Sciences 68, 248–268.

Vauchez, A., Egydio Silva, M., Babinski, M., Tommasi, A., Uhlein, A., Liu, D., 2007. Deformation of a pervasely molten middle crust: insights from the Neoproterozoic Ribeira-Araçuaí orogen (SE Brazil). Terra Nova 19, 167–186.

Vavra, G., Schmid, R., Gebauer, D., 1999. Internal morphology, habitat and U-Th-Pb microanalysis of amphibolite-to-granulite facies zircons: geochronology of the Ivrea Zone (Southern Alps). Contributions to Mineralogy and Petrology 134, 380–404.

Vielzeuf, D., Montel, J.M., 1994. Partial melting of metagreywackes. Part I. Fluid-absent experiments and phase relationships. Contributions to Mineralogy and Petrology 117, 375–393.

White, R.W., Powell, R., 2002. Melt loss and the preservation of granulite facies mineral assemblages. Journal of Metamorphic Geology 20, 621–632.

White, R.W., Powell, R., Holland, T.J.B., Worley, B.A., 2000. The effect of TiO_2 and Fe_2O_3 on metapelitic assemblages at greenschist and amphibolite facies conditions: mineral equilibria calculations in the system $K_2O–FeO–MgO–Al_2O_3–SiO_2–H_2O–TiO_2–Fe_2O_3$. Journal of Metamorphic Geology 18, 497–511.

White, R.W., Powell, R., Holland, T.J.B., 2001. Calculation of partial melting equilibria in the system $Na_2O-CaO-K_2O-FeO-MgO-Al_2O_3-SiO_2-H_2O$ (NCKFMASH). Journal of Metamorphic Geology 19, 139–153.

White, R.W., Powell, R., Clarke, G.L., 2002. The interpretation of reaction textures in Fe-rich metapelite granulites of the Musgrave Block, Central Australia: constraints from mineral equilibria calculations in the system $K_2O–FeO–MgO–Al_2O_3–SiO_2–H_2O–TiO_2–Fe_2O_3$. Journal of Metamorphic Geology 20, 41–55.

White, R.W., Powell, R., Halpin, J.A., 2004. Spatially-focussed melt formation in aluminous metapelites from Broken Hill, Australia. Journal of Metamorphic Geology 22, 825–845.

White, R.W., Powell, R., Holland, T.J.B., 2007. Progress relating to calculation of partial melting equilibria for metapelites. Journal of Metamorphic Geology 25, 511–527.

Whitney, D.L., Evans, B.W., 2010. Abbreviations for names of rock-forming minerals. American Mineralogist 95, 185–187.

Yakymchuk, C., Brown, M., 2014. Consequences of open-system melting in tectonics. Journal of the Geological Society 171, 21–40.